

## Article

# Computational Analysis of Enhanced Circulating Tumour Cell (CTC) Separation in a Microfluidic System with an Integrated Dielectrophoretic-Magnetophoretic (DEP-MAP) Technique

Wan Shi Low \* and Nahrizul Adib Kadri

Department of Biomedical Engineering, Faculty of Engineering, University of Malaya, 50604 Kuala Lumpur, Malaysia; drirwan1@um.edu.my

\* Correspondence: low89shi@gmail.com; Tel.: +60-379-676579

Academic Editor: Igor Medintz

Received: 4 March 2016; Accepted: 22 July 2016; Published: 18 August 2016

**Abstract:** Cell based cancer analysis is an important analytic method to monitor cancer progress on stages by detecting the density of circulating tumour cells (CTCs) in the blood. Among the existing microfluidic techniques, dielectrophoresis (DEP), which is a label-free detection method, is favoured by researchers. However, because of the high conductivity of blood as well as the rare presence of CTCs, high separation efficiency is difficult to achieve in most DEP microdevices. Through this study, we have proposed a strategy to improve the isolation performance, as such by integrating a magnetophoretic (MAP) platform into a DEP device. Several important aspects to be taken into MAP design consideration, such as permanent magnet orientation, magnetic track configuration, fluid flow parameter and separation efficiency, are discussed. The design was examined and validated by numerical simulation using COMSOL Multiphysics v4.4 software (COMSOL Inc., Burlington, MA, USA), mainly presented in three forms: surface plot, line plot, and arrow plot. From these results, we showed that the use of a single permanent magnet coupled with an inbuilt magnetic track of 250  $\mu\text{m}$  significantly strengthens the magnetic field distribution within the proposed MAP stage. Besides, in order to improve dynamic pressure without compromising the uniformity of fluid flow, a wide channel inlet and a tree-like network were employed. When the cell trajectory within a finalized MAP stage is computed with a particle tracing module, a high separation efficiency of red blood cell (RBC) is obtained for blood samples corresponding up to a dilution ratio of 1:7. Moreover, a substantial enhancement of the CTCs' recovery rate was also observed in the simulation when the purposed platform was integrated with a planar DEP microdevice.

**Keywords:** dielectrophoresis; magnetophoresis; circulating tumour cells; COMSOL; numerical analysis

## 1. Introduction

In clinical practice, cancer diagnostics are commonly performed through radiological imaging modalities such as traditional radiography (X-ray), magnetic resonance imaging (MRI), computed tomography (CT), positron emission tomography (PET) or ultrasound [1]. These techniques allow visualization of the internal body structure, thus enabling physicians to delineate the group of tumour cell colonization. However, there are some drawbacks to these techniques. For instance, the deficiencies of resolution in imaging modalities have precluded them from imaging small numbers of cancer cells before angiogenic switch, which in turn limits the detection sensitivity [2,3]. Furthermore, most of the cases are normally diagnosed at advanced stages where patients often relapsed within 24 months of therapeutic intervention [4,5].

The discovery of circulating tumour cells (CTCs) as a precursor to the formation of secondary tumours has shed some new light in clinical prognosis. These cells are believed to have undergone cellular transformation that caused them to lose their cell polarity and cell-cell adhesion via increased mobility and invasiveness, to enter into the bloodstream [6]. Its clinical significance was augmented when a study conducted by Husemann et al. highlighted that CTCs can be found in patients even before a primary tumour is detected with conventional clinical screening methods [4]. Furthermore, prospective multicentre studies reported that patients with the presence of 5 CTCs per 7.5 mL of blood would have poor survival rates [7,8]. Accordingly, this finding has highlighted the prognostic value of CTC enumeration in correlating progression-free survival and overall survival of patients with metastatic carcinoma. As a result, the enumeration of CTC from blood of a cancer patient can serve as an important biomarker for real-time prognosis thus precluding recurrences and metastatic relapses. Despite this clinical relevance, the detection and analysis of CTCs are extremely difficult due to their rare appearance in blood. For comparison, there are approximately 1 to 10 CTCs within 1 mL of blood which contains a few million white blood cells and a few billion red blood cells. Furthermore, CTCs' highly heterogeneous morphologies which are distinct from the profiles of single cells from cancer cell lines have made the isolation process technically challenging [9–12]. Thus, a highly sensitive detection device is needed to accurately characterize and enumerate CTCs.

The selection of a microfluidic sorting system can be divided into two broad categories: the biochemical-enhanced method and the label-free method. The biochemical-enhanced method differentiates CTCs from other blood cells based on their immune-affinity properties [9]. However, as the knowledge of specific and unique antigens that can distinguish CTCs from hematopoietic stem cells is limited, this technology may potentially miss CTCs that have undergone a transition to be less-expressive or if they completely lose certain antigens [5]. Meanwhile, the label-free method isolates cells mainly based on their intrinsic bio-physical properties, such as size, deformability, and electric conductivity [13]. Examples of these techniques include microfiltration [14,15], hydrodynamic sorting [16,17] and dielectrophoresis [18,19]. Since CTCs are unmodified by physical separation, cells isolated using these techniques are compatible with a wider range of downstream phenotypic and genotypic analyses, including those requiring viable cells. Despite their popularity in CTC research, there are some issues which arise in the size-based microfluidic separation method, particularly of microfiltration and hydrodynamic cell sorters. A study conducted by Park et al. showed that a significant overlap in size of certain CTCs with leukocytes resulted in leukocyte contamination [20]. In addition, as the effectiveness of these size-based microfluidic devices are controlled by tailored gap dimensions, their separation mechanisms are not universal and will require variation in design when the target sample changes. In contrast to size-based microfluidic separation, dielectrophoresis (DEP) utilizes an external electric field source to manipulate the CTC separation within the microchannel. This technique allows the reconfiguration of the electric field externally to obtain accurate isolation results in accordance with cell phenotypes, thereby promoting flexible control of the microenvironment for a wide range of cells. Furthermore, several studies discovered that most CTCs exhibit similar responses when they are subjected to an electrical field in spite of their heterogeneity [19]. Consequently, it has been surmised that DEP can be used to detect CTCs of different cancer types. This technique is thus employed to develop a microfluidic platform for CTC isolation in this study.

Generally, DEP refers to a net force on the dielectric particles in response to a spatially non-uniform electric field. The expression for the DEP force can be represented by:

$$\vec{F}_{DEP} = 2\pi\epsilon_0\epsilon_m R^3 \text{Re}[K(\omega)] \nabla E^2 \quad (1)$$

where  $\nabla E$  is the magnitude gradient of electric field, expressed in RMS value and  $K(\omega)$  denotes the complex Clausius-Mossotti factor. Leveraging the dissimilarities of electrical properties between CTCs and blood cells, few bench-top DEP devices have been successfully used to detect variables of cancer cells, including oral [21,22], colon [23], breast [19], lung and prostate cancer cells [24].

Although the discussed DEP technique shows a successful CTCs' isolation outcome, there are some limitations reported across multiple studies. First and foremost, for an on-chip DEP microfluidic device, the reported separation efficiency is relatively low, such that the achievable recovery rate for cancer cells is less than 80%. Such a scenario is mainly caused by the high conductivity of blood [25]. This distinctive blood feature has resulted in cells experiencing negative DEP most of the time, and therefore influencing the separation performance of a DEP device (e.g., difficult to obtain a high purity output) [26]. Additionally, the high conductivity of a blood suspension is reported to cause significant heating within a DEP device. This may lead to undesirable lysing of cells [26,27].

As first noted by Gascoyne et al. [28], the integration of multiple separation forces enables a microfluidic device to precisely control the cell separation dynamics, and thus give rise to new modalities of separation. In order to improve CTC capture efficiency as well as to achieve the isolation of cell types having small differences in their DEP crossover frequencies, integration of DEP with other cell separation techniques has been attempted. Up-to-date, there is only one method, known as hydrodynamic separation technique, which has been reported to be integrated with a DEP-based microfluidic chip for CTCs' isolation. This technique is pioneered by a group of scientists from the University of Texas MD Anderson Cancer Centre's Laboratory Diagnostic Microsystems (Houston, TX, USA), whereby they combined the DEP force with field-flow fractionation to create DEP-FFF [29]. In this approach, a diluted mixed cell population which continuously flows into the chamber, is subjected to a combination of upward-pushing DEP force, downward-pulling sedimentation force, and hydrodynamic force. When the preliminary performance of DEP-FFF is tested using human blood sample spiked with breast cancer cell line (MDA-MB-231), Gupta et al. demonstrated a recovery efficiency of 86.6% [30]. Therefore, it can be deduced that the development of DEP-FFF has enhanced cell discriminating ability and throughput in contrast to a standalone-DEP stage.

Despite enhanced separation, there are numerous problems to be solved in this integration platform. The latest study conducted at BEACON indicated an existence of excessive cell loading in the DEP-FFF device [31]. Such a condition can result in dipole-dipole interaction between cells, thus causing the clustering of cells and the entrapment of both similar and dissimilar cell types. Consequently, it will reduce the separation efficiency of a device. For example, on a DEP-FFF device which consists of arrays of 50  $\mu\text{m}$  wide interdigitated electrodes, the isolation efficiency is 85% at a loading density of 500 peripheral blood cells per  $\text{mm}^2$  but only 20% at a loading density of 10,000 peripheral blood cells per  $\text{mm}^2$  [32]. However, it should be noted that the number of target CTCs in clinical specimens is very small. The overloading of cells within the DEP chamber which might cause interactions between CTCs does not have any impact on device performance. From a CTC application standpoint, such a condition is undesirable as it shows the isolation efficiency of CTCs is independent of their concentration. Though few studies suggested that the overloading cell problem can be solved by increasing a blood dilution ratio, Pommer et al. [33] and Liao et al. [34] reported that the actual separation efficiency dropped approximately 20% if a dilution ratio of 1:10 of the whole blood sample was carried out. Furthermore, another study conducted by Takaori in 1966 indicated that an excessive dilution will cause a progressive decrease in the blood sample pH [35]. Since blood cells respond quickly to the changes in their environment, their biological characteristics might change in regard to the reduction of pH.

To circumvent these issues, integration of DEP with another cell separation force will be attempted. The design will focus on decreasing an excessive cell loading within a DEP separation chamber, as well as enhancing recovery rate and throughput. Notably, in a whole blood sample, 98% of human blood cells are red blood cells (RBCs), whose cell density is around  $5 \times 10^6$  cells/ $\mu\text{L}$  [36]. Besides, a study conducted by a group from LifeScan Scotland showed that electrical conductivity of the blood medium is highly dependent on the haematocrit level within the blood [37]. As such, the blood medium conductivity will be reduced with the decreased of haematocrit level. Therefore, a removal of RBCs from a whole blood sample in the early stage would greatly help downstream sub-classification of target cells as well as to eliminate cell overloading issues. In the literature, centrifugation has been employed as a pre-enrichment step prior to sorting by DEP. However, previous

studies have shown that the blood sample tends to mix with the gradient media if the centrifugation is not performed immediately after applying it to a sample. Besides, excessive cell loss might occur as a consequence of density-medium-related cytotoxicity [38]. Importantly, this technique is found to stress cells for an extended period, which might activate the white blood cells [39]. Such activation will alter the protein and gene expression pattern of white blood cell (WBC), thus limiting the downstream application for DEP.

Interestingly, various studies have reported RBCs to exhibit a distinctive magnetic response under a magnetic field in contrast to both WBC and CTC. The presence of iron-containing molecules, such as haemoglobin within RBC has resulted in it behaving as a paramagnetic microparticle when subjected to an inhomogeneous magnetic field. CTC and WBC, on the other hand, are found to be lacking in iron-manganese-containing molecules which behave as diamagnetic microparticles, such that the cells are repelled from the high magnetic field gradient [40]. Owing to this feature, a technique which employs non-uniform magnetic field in cell separation, namely magnetophoresis (MAP) is proposed in this study as a pre-enrichment stage of the DEP separation system. Despite relatively few MAP systems having been developed for RBC separation, studies have shown promising results with approximately 90% RBC recovery with this method [41–43]. Its equation can be written as:

$$\vec{F}_{MAP} = \int_V \left( \vec{M} \cdot \vec{\nabla} \right) \vec{B}_{ext} d\vec{V} \quad (2)$$

where,  $V$  is the volume of a cell,  $M$  denotes the resulting magnetization of the material,  $\nabla$  is the gradient operator, and  $\vec{B}_{ext}$  is the magnitude of the external magnetic flux density.

Notably, a precise control of the cell's microenvironment in a microfluidic system still remains a vexing challenge within the technological realm. In this case, computational modelling could serve as a decision-making tool for researchers by providing an order of magnitude estimate of the potential chip performance, thus enabling a fruitful path to be taken from the beginning of the experiment. Henceforth, in the course of this study, a computational model, which primarily focuses on design and development of the MAP stage, will be generated with COMSOL Multiphysics to assist the design choices and to confirm the analytical results by gaining further insight into the produced magnetic field phenomena within our proposed microfluidic platform. As our design features continuous flow, the parameters such as sample size, surface-to-volume, and hydrodynamic force are also addressed to help develop a uniform velocity flow within the microfluidic channel that encourages better cell distribution for integrated MAP and DEP application. A detailed description of the requirements is given in Supplementary Section 1. In order to validate the feasibility of separating blood cells in a continuous flow environment, a computational experiment is conducted using a particle-tracing module. Its cell trajectory analysis is implemented based on the Lagrangian-Eulerian numerical approach that takes into account magnetic, electric, and hydrodynamic forces. Based on the result of the simulation, our study outlines the best geometrical design of the MAP stages in order to facilitate CTC separation for downstream DEP analysis. At the end of this research, an integrated MAP-DEP device is examined, whereby the DEP platform design is adapted from a study conducted by Moon et al. [19]. To the best of our knowledge, there are no benchmark datasets for the integration of DEP and MAP for CTCs' isolation.

## 2. Computational Modelling Method

Our computational analysis focused on the MAP stage, whereby the evaluated properties include permanent magnet orientation, measurement of magnetic field gradient across the ferromagnetic track, hydrodynamic mechanism, separation efficiency, and dilution ratio (see Supplementary Section 2 for details). By assembling these parameters in algorithms, a separation can be computationally tested and calibrated to achieve optimal recovery rate and throughput. Generally, the computational fluid dynamics method was conducted using the finite analysis package COMSOL Multiphysics 4.4<sup>®</sup> (COMSOL Inc., Burlington, CA, USA). It is a modelling software which consists of advanced physical simulation platform as well as visualization tools to treat fluid structure interaction within our

microfluidic architecture. It was used to perform numerical methods with a primary focus on MAP and DEP equation for both 2D and 3D design in our study. The aim of 2D modelling was to validate the forces within the proposed microchannel, while the 3D modelling was employed to compute particle trajectory. To perform the numerical analysis, several assumptions as written below were made:

- The fluid injected at the inlet channel is non-Newtonian, whereby the viscous stress that arises from the flow is linear at every point.
- Cells are spherical.
- The flow within the microfluidic is incompressible such that it has constant density, viscosity, and concentration.
- As the cross sectional of the microchannel is less than  $1 \text{ mm}^3$ , the Reynolds number generated within the fluid flow is less than 200. Therefore, the flow is considered laminar.
- Blood clotting did not occur within the microchannel.
- Both the surrounding medium and the system are considered to have uniform bulk conductivities, dielectric constants, and magnetic permeability. Hence no space charge with the system.
- The fluid has constant electric conductivity and magnetic permeability.
- A constant magnetic field gradient is generated across the fluid volume in the MAP stage. The electric conductivity is negligible in this stage.
- The magnetization of cells is collinear with the magnetic field.
- The presence of a non-magnetic cell does not distort the magnetic field lines in the MAP stage.
- Joule heating and electrochemical effects are assumed negligible in the DEP stage. This is because the electric field is low and the frequency is high.
- Cells flow according to the fluid stream. They do not stick to the boundaries.

The proposed microfluidic geometry is available in Supplementary Section 3. Prior to generating the 2-D COMSOL simulation model, the CAD model of the microfluidic architecture was created. It was performed by using AutoCAD® 2013 (Autodesk Inc., San Francisco, CA, USA) due to its ability to generate complicated designs and its compatibility with COMSOL Multiphysic. The design geometry was then imported into the COMSOL model library. Notably, in order to generate the 3D model, the desired work plane had first to be indicated before the imported 2-D geometry was located on it. Subsequently, the 2-D cross section layout was extruded in the Z direction to form a 3-D structure. After completing the geometry for our proposed model, the materials of the domains were defined accordingly. In this case, the property function of each material was complemented by the COMSOL Material Library. To attain a more realistic device design, the physical parameters of blood cells associated with both the MAP and DEP device were obtained from the literature as described in Table 1 [33,44–46]. These parameters were directly accounted in our resulting computation. Notably, both breast and prostate CTC are of interest in this study in which breast CTCs have the largest size in CTC taxonomy [19,46,47] and vice versa for prostate CTCs [48–50].

**Table 1.** The dielectric and magnetic parameters of cells used for device modelling.

Cell Type	Mean Radius, $r$	Magnetic Susceptibility, $\chi_{\text{cell}}$	Electrical Properties	
			$\sigma_{\text{cytoplasm}}$ (S/m)	$\epsilon_{\text{cytoplasm}}$
Red blood cell (RBC)	4	$-3.69 \times 10^{-6}$	0.52	57
White blood cell (WBC)	7	$-9.9 \times 10^{-6}$	0.76	150.9
Human breast cancer MDA-231	20	$-9.5143 \times 10^{-6}$	0.62	52
Human prostate cancer HeLa	7.36	$-9.4966 \times 10^{-6}$	0.21	52
Platelet	2	$-9.2 \times 10^{-6}$	0.25	$1 \times 10^{-7}$

In the COMSOL model builder, a complex system of points was presented to highlight the stress levels of a particular area. Generally, regions which normally have higher node density received large amounts of stress compared to those with lesser node density. Generation of mesh happened when these points were connected according to nodal point number. It was also programmed to define the



flow simulation properties within the microfluidic channel. To avoid inverted mesh elements, the size of mesh had to be very fine around the region where remeshing occurred (such as the curved region of the channel). This was accomplished by using “Free Mesh Parameters”, whereby the size of mesh was set to “predefined”. To obtain an accurate solution with a mesh that was sufficiently dense and not overly demanding of computing resources, a “Convergence Study” was performed using “Physic Induced Sequence Setting”. The results were found to converge satisfactorily when a maximum element size of  $5 \times 10^{-5}$  was stipulated for the fluidic channel subdomain.

Subsequently, the finite element method analysis was implemented using three main modules, including: magnetic field, electric field, and Navier-Stokes module. The result obtained from the magnetic field ( $H$ ,  $M$ ,  $\frac{\partial H}{\partial X}$ ,  $\frac{\partial H}{\partial Y}$ ,  $\frac{\partial H}{\partial Z}$ ) and electric field simulation ( $E$ ,  $\frac{\partial E}{\partial X}$ ,  $\frac{\partial E}{\partial Y}$ ,  $\frac{\partial E}{\partial Z}$ ) was taken as input for the particle tracing module to generate the cell trajectory within the proposed microchannel. A detailed flow chart of the modelling approach for the proposed micro-device is depicted in Figure 1. Additional details of how the computational mode was built and validated are included in the Supplementary Section 4.

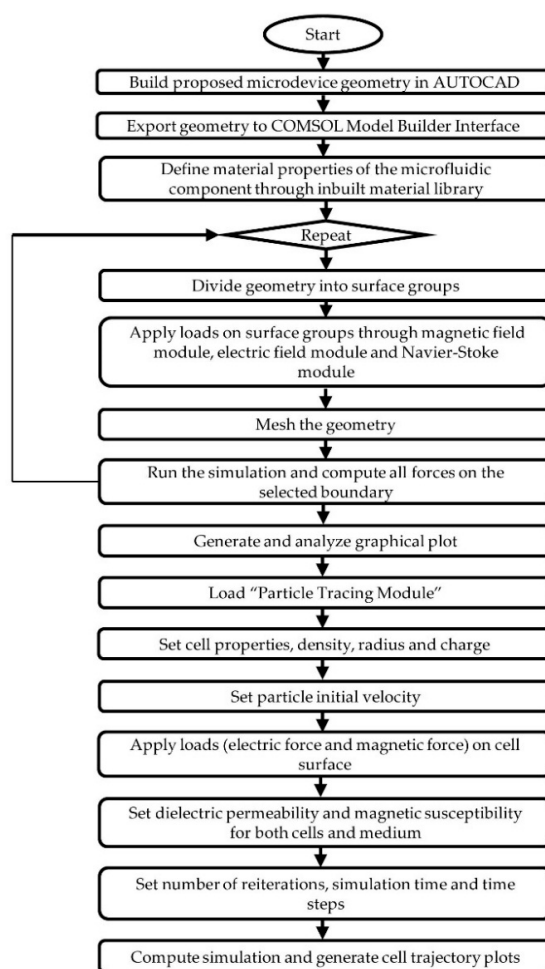


Figure 1. Detailed flow chart of our simulation approach.

### 3. Results and Discussions

#### 3.1. Magnetophoresis Stage

In this section, we study the effect of magnetic field caused by various placements of the permanent magnet as well as the use of a ferromagnetic track. The geometrical design of the MAP chamber which accommodates uniform flow as well as optimized magnetic field distribution is investigated. For the purpose of this analysis, the design concept focuses solely on the MAP stage.

A permanent magnet with dimension of 15 mm × 10 mm × 10 mm was employed in our computational study. Notably, its length is determined accordingly to the length of the MAP microchamber.

### 3.1.1. Permanent Magnet Configuration: Conventional vs. Face-to-Face Permanent Magnet

Three references of permanent magnet configurations as mentioned in Supplementary Section 3.1.1 were studied. For the conventional method, a magnet was located 5 mm from the microfluidic channel and was simulated as having a positive magnetization. Meanwhile, the face-to-face magnet configuration was surrounded by two permanent magnets, 5 mm from the microchannel wall at each side. As mentioned in Supplementary Section 1, the ratio of magnet length to magnet inter-gap distance for the face-to-face magnet configuration has to be more than 1. In this design, the calculated ratio is  $\frac{15}{10+0.75} = 1.395$ , thus fulfilling one of our design requirements. To generate an attractive magnet orientation as notified in Figure S2b (refers to Supplementary materials), the magnetization of both permanent magnets were configured as positive. Conversely, for the repulsive magnet configuration (see Figure S2c), the magnetization of both magnets were computed to have opposite signs. A distribution of magnetic flux density generated from these magnet configurations is presented in surface plots, as depicted in Figure 2.

Figure 2a–c shows the 2D surface plot of magnetic flux density (**B**) of the discussed permanent magnet configuration. To illustrate the direction of the magnetic field in each model, an arrow plot of the magnetic field lines was coupled on each surface plot. In Figure 2a, a uniform magnetic flux density, which was represented by an evenly blue spectrum, was found within the microchannel when the single permanent magnet configuration was applied. Meanwhile, in both attraction (Figure 2b) and repulsion (Figure 2c), the fluctuation of magnetic flux density is observed to be higher at the microchannel region which is aligned at the midpoint ( $x = 10$ ) between both permanent magnets. Note that the cell separation takes place in the MAP microchamber. It refers to the region which is located parallel to the permanent magnet that ranges from  $x = 2.5$  to  $x = 17.5$ . To quantitatively evaluated magnetic flux density within this region, 3D surface charts with contour plots projected onto  $x$ - $y$  plane, were plotted across the length ( $x$ -axis) and the width ( $y$ -axis) of the microchannel.

As shown in Figure 2d, the magnetic flux gradient of the single magnetic configuration is found to be orientated toward  $y$ -axis, whereby it gradually decreases from 0.12 T to 0.104 T. This situation can be defined through the inverse square law, which states that **B** is inversely proportional to the distance from the permanent magnet squared [51]. On the contrary, the magnetic flux density for both the attractive (see Figure 2e) and repulsive configurations (Figure 2f) was found to be orientated along the length of the magnet ( $x$ -axis). A symmetry axis was presented at  $x = 10$  mm for both configurations. For instance, in Figure 2e, the attractive configuration generates a high spectrum value of 0.22 T in the middle region ( $x = 10$  mm) along the microchannel length and gradually decreases toward the region next to the edge of the permanent magnet. Meanwhile, the repulsive configuration, as depicted in Figure 2f, displays a mirror 3D surface image of attractive configuration. These observed phenomena within the microchannel for both the attractive and repulsive configuration can be explained by referring to the direction of the arrows. As shown in the arrow plot, the magnetic lines travel from north (N) pole directly to the south (S) pole. Therefore, in an attractive magnet configuration, the magnetic lines from N pole go directly to the S pole confronting it. Consequently, a high magnetic scalar field (represented by red spectra) was found in the middle zones of the microchannel. It gradually decreased toward inlet and outlet, forming a loop around the magnets. Unlike attraction, the repulsive magnet configuration has two positive forces, facing each side of the microchannel wall. Henceforth, this configuration compels the magnetic field lines to turn horizontally before the horizontal symmetry axis of the microchannel. As a result, a low (shorter arrow) field region and two focusing zones with high magnetic field were detected respectively in the middle of the microchannel and the corners of both magnets.

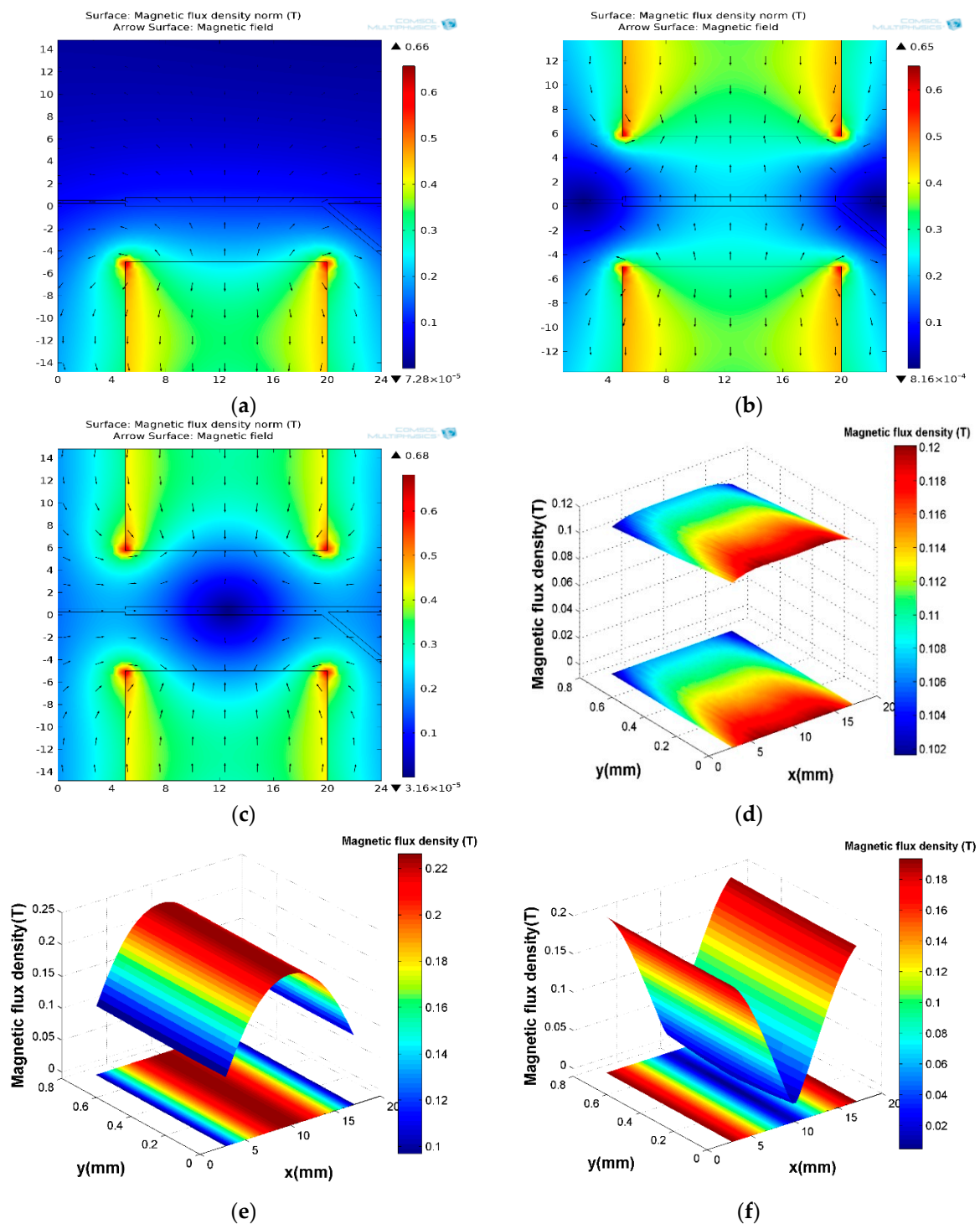


**Figure 2.** Schematic of surface plot and arrow plot of magnetic flux density: (a) Single magnet configuration; (b) Attractive magnet configuration; (c) Repulsive magnet configuration; The distribution of magnetic flux density within the microchannel for each model was plotted in a 3D surface plot at the bottom of surface plot, with the contour plot projected onto the  $x$ - $y$  plane, labelled as (d–f).

In the process of further validating our result, a post-processing of particle trajectories within the microfluidic channel was implemented. For this model setting, a steady state study was employed whereby an initial condition of the cell was assigned to align along the length of the microfluidic channel, at a constant distance of  $5 \mu\text{m}$  from each other. The resulted plot is delivered in Figure 3,



whose equalities of forces were simulated according to Equation (2). To ease the analysis process, a grey-scaled magnetic field surface is set as the plot background, as such the high magnetic flux density (**B**) region is represented by light grey and the colour saturation increases with decreasing of **B**.

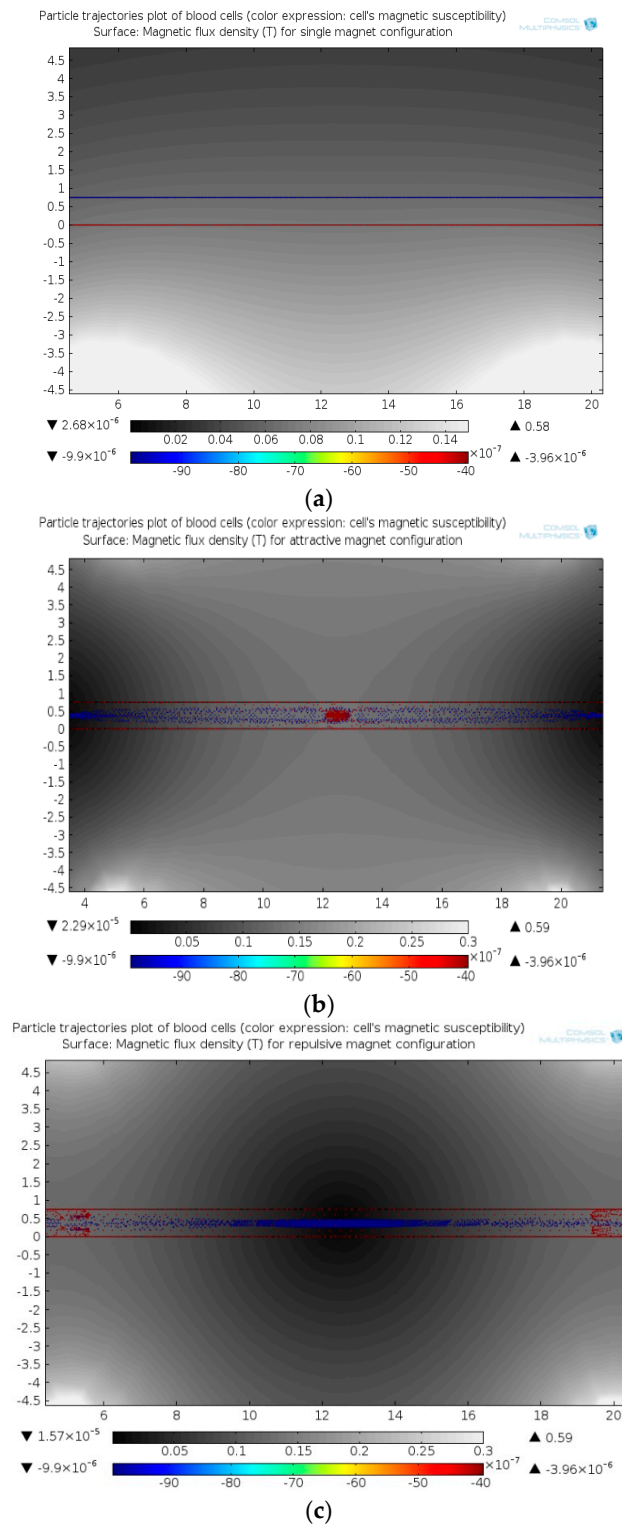


**Figure 3.** Cell trajectories within the microchannel: (a) Single magnet; (b) Magnet in attraction; (c) Magnet in repulsion. The grey scale and colour spectrum bar showed the magnetic flux density and magnetic susceptibility of cells, respectively.

In Figure 3, the red particles represent the RBCs meanwhile other nucleated blood cells such as CTCs and WBCs (whose magnetic susceptibility is lower than  $-8 \times 10^{-6}$ ) are represented by blue particles. For a single permanent magnet configuration, the cells were found to move toward both sides of the channel walls. As shown in Figure 3a, RBCs are attracted towards the channel wall located next to the permanent magnet (high  $\mathbf{B}$  region), thus exhibiting p-MAP. Meanwhile, n-MAP driven cells such as CTCs, WBCs and platelets were found to be repelled toward the opposite channel wall with low  $\mathbf{B}$  value. On the contrary, the presence of an axially-symmetric magnetic flux density within the attractive and repulsive configuration resulted in various cells accumulating in the middle region of our proposed MAP microchamber. For instance, in Figure 3b, accumulation of RBC was found around this region due to the presence of high magnetic field. Likewise, Figure 3c showed n-MAP-driven cells to be concentrated around the middle of the microchannel due to the presence of low  $\mathbf{B}$  zone. Considering the influence of the magnet orientation, both attractive and repulsive configuration will cause cell blockage within the microchannel thus compromising the purpose of our MAP stage. Since a single permanent magnet generates two opposing  $\mathbf{B}$  along the left-right microchannel wall respectively, coupled with the hydrodynamic force, the cells can be separated and directed toward the desired outlets at the end of the MAP stage. Henceforth, this configuration is selected to generate the magnetic force in our proposed MAP stage.

### 3.1.2. Ferromagnetic Track's Configuration

It has been shown that the magnetic field and force is restricted to a specific location defined by the magnet pole orientation. In order to overcome the low magnetic forces on biological cells (see Supplementary materials), a rectangular ferromagnetic track which was made of NiFe (Permalloy) element, was embedded inside the microchannel of our simulated MAP stage. This element allowed the bias magnetic field to be locally amplified into the microchannel, thus giving rise to a magnetic force on the cells flowing through it. The length and height of this track was designated as 14.5 mm and 0.5 mm, respectively. Meanwhile, its width was fixed at 0.25 mm due to the limitation in our laboratory. As illustrated in Figure 1a, the enlarging field lines at the magnet extremities has resulted in a decrease in the magnetic flux magnitude at the region parallel with the permanent magnet edges. To allow a uniform distribution of the magnetic field line to permeate through the ferromagnetic track, the permanent magnet has to cover the length of the track. A new length of 20 mm was therefore designated for the magnet in our study. The schematic of the microchannel with ferromagnetic track for the MAP stage is illustrated in Figure 4a. All dimensions used are in millimetres.

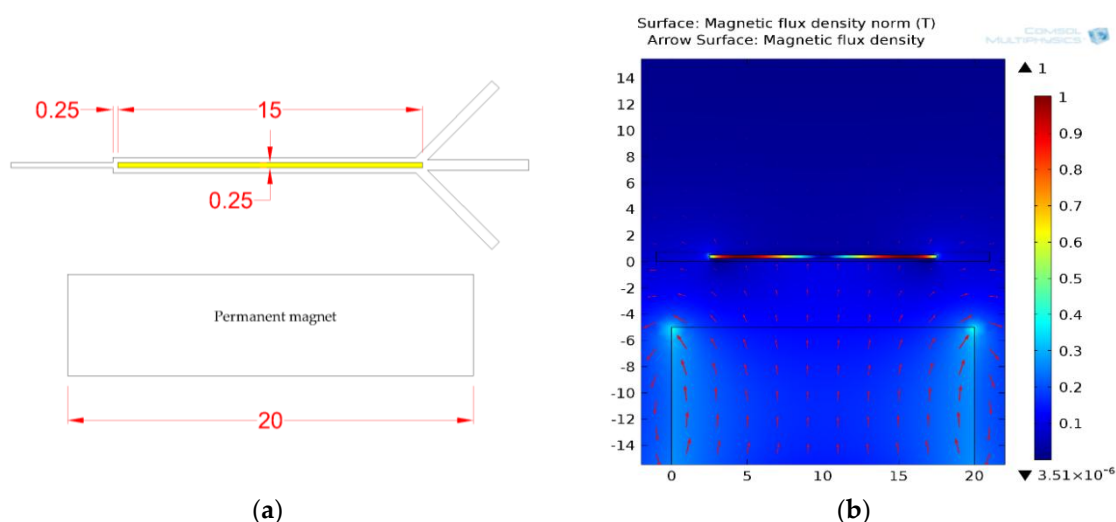
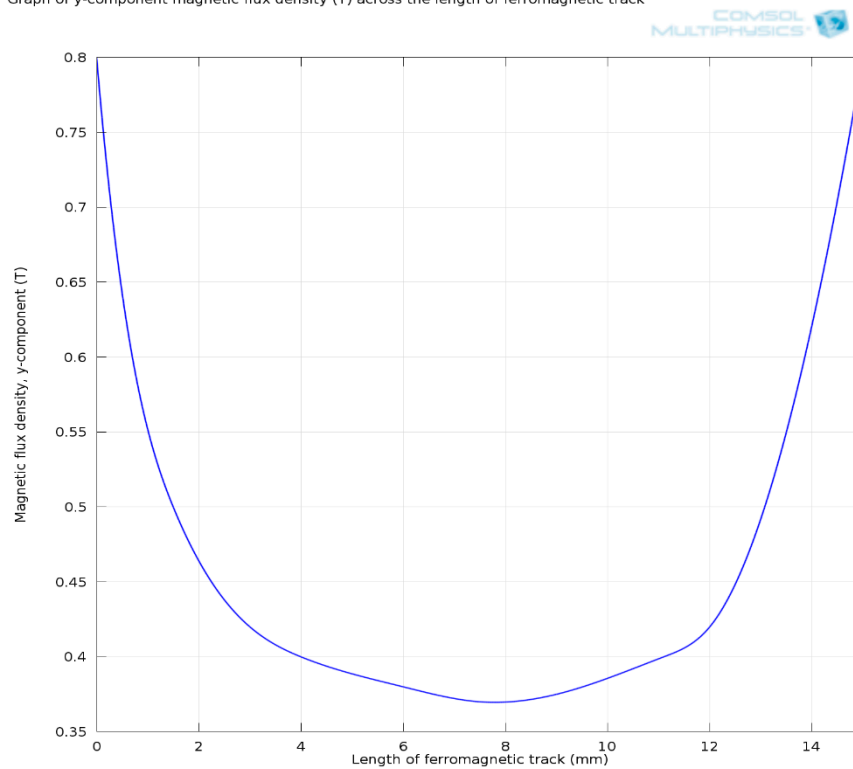


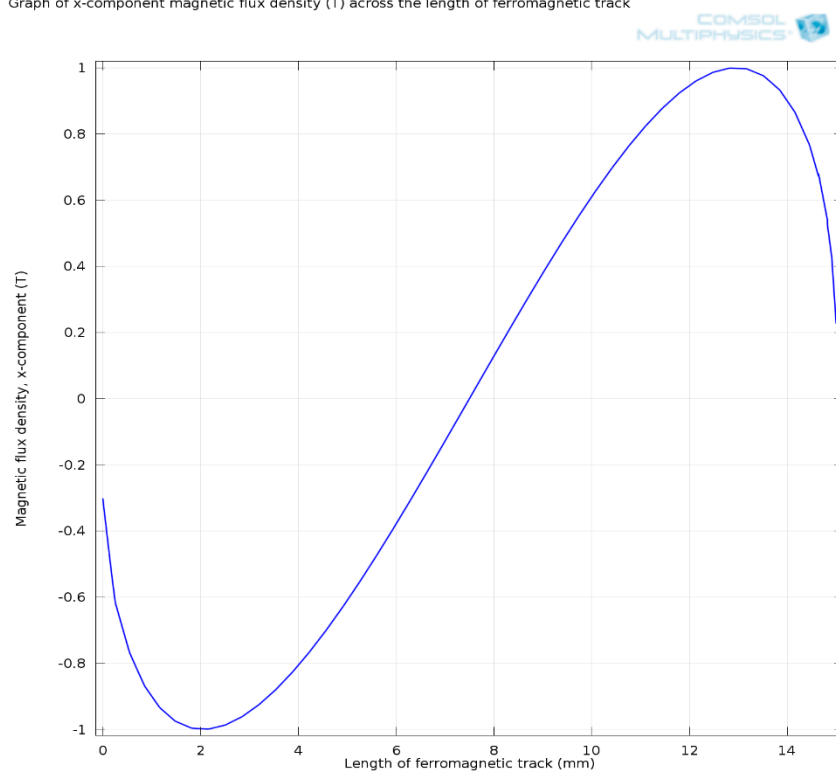
Figure 4. Cont.

Graph of y-component magnetic flux density (T) across the length of ferromagnetic track



(c)

Graph of x-component magnetic flux density (T) across the length of ferromagnetic track



(d)

**Figure 4.** (a) Schematic of microchannel with ferromagnetic track (yellow region) in the MAP stage. Its magnetic flux density analysis is presented by the (b) surface plot. Graph of magnetic flux generated within the ferromagnetic track vs. the length of the track is plotted for: (c) y-component; (d) x-component.

The distribution of the magnetic field for the updated geometry is depicted in Figure 4b–d. In the presence of the magnetic track, the external flux provided by the permanent magnet magnetised the ferromagnetic track. It was reported in a previous study that the magnetic domain of a ferromagnetic element operated linearly with the magnetic flux which permeated through it [41]. Consequently, the magnetic moments will be aligned with one another, thus causing the magnetic field lines to be focused through the track. This phenomenon is illustrated via the arrow plot in Figure 4b. Due to the presence of concentrated field lines, a high field pattern (represented by the red region) was found within the ferromagnetic track. Note that there is a low field pattern presented in the middle region of the proposed track. The reason for such a condition is caused by the flowing loop of magnetic field lines within the ferromagnetic track. This low field phenomenon can be explained by plotting the  $x$ -component ( $B_x$ ) and  $y$ -component ( $B_y$ ) of the magnetic flux density across the length of the embedded track. The plotted line graphs are shown in Figure 4c,d, respectively.

In Figure 4c, the  $B_y$  is found to be uniform along the middle region of the ferromagnetic track, with an average of 0.35 T. The value was increased to 0.8 T towards the edge of the track. It is caused by the field line concentration effect as a result of the high surface-area-to-volume ratio at this coordination. Likewise, Figure 4d also displayed a high  $B_x$  at the edge of the ferromagnetic track. However, centring at the middle point of this track, the magnitudes obtained at both edges were opposite to each other. This phenomenon results from the magnetic ordering of the atomic moment within the ferromagnetic track, whereby the dipoles spontaneously align parallel in response to the closed-looped flow direction of magnetic flux from a single permanent magnet [52]. Subsequently, the magnetic dipoles which were present at the centre region of the ferromagnetic track were nullified by other dipoles which aligned antiparallel to it and therefore zero  $B_x$ . Notably, on a cross section with constant  $z$  direction, the magnetic flux density,  $B$  is equal to the square root of the flux density in both  $x$  and  $y$  direction, such that:

$$B = \sqrt{B_x^2 + B_y^2} \quad (3)$$

By relating this equation to both Figure 4c,d, the surface plot obtained in Figure 4b can thus be justified.

In order to ensure the acquired MAP force will be sufficient to deviate the cells toward the high and low magnetic flux density region within a continuous flow, the  $B_y$  which was generated across the channel width was examined. As illustrated in Figure 4c, the distribution of  $B_y$  along the length of the ferromagnetic track is symmetrical to the  $y$  axis. To ease the analysis process, the comparison was implemented on  $B_y$  at three surface cross sections, which were labelled as I, II and III (see Figure 5a). In this case, I refers to the cutline across the microfluidic channel at the edge of a ferromagnetic track. Meanwhile, II and II represent the cutline at the quarter points and midpoints of the track, respectively. A graph of  $B_y$  across channel width at these surface cross-sections is delivered in Figure 5b.

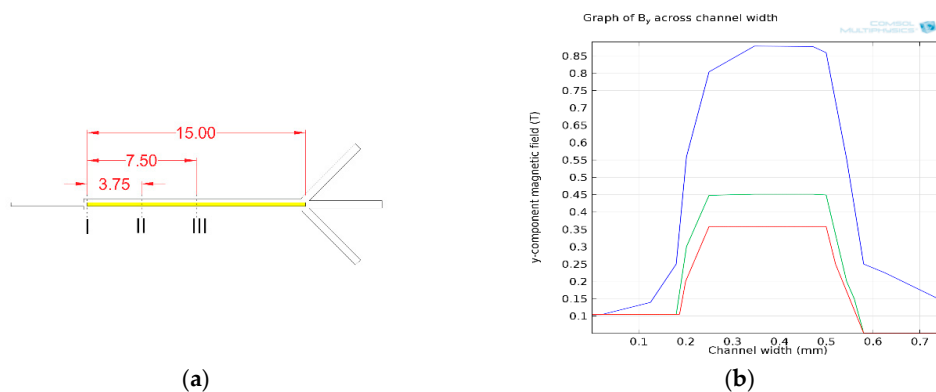


**Figure 5.** (a) Y-component magnetic field analysis at cross section within the microfluidic channel labelled as I, II and III; (b) The distribution of  $B_y$  was plotted across the channel width.

From Figure 5b, the three cutlines display similar trends in the plotted line graph such that a maximum of the magnetic field was obtained at the region within the ferromagnetic track and a minimum magnetic field was found at the fluid-flowing channels. When an external magnetic field ( $\mathbf{B}_{\text{ext}}$ ) was applied toward the microchannel, the difference of net magnetization ( $\mathbf{M}$ ) between the permanent magnet and the magnetic track caused the sample in the region bounded by  $x = 0$  to  $x = 0.24$  to be rotated by the torque in an equilibrium direction which was along the  $y$  axis in our study. Consequently, a uniform distributed magnetic field was obtained in this region. Due to the presence of a strong localized field within the ferromagnetic track, the magnitude of  $\mathbf{B}_y$  was found to increase and reached its maximum value in the region bounded by  $x = 0.25$  to  $x = 0.5$ . Interestingly, a plateau region of magnetic field was presented within the ferromagnetic track. Such a condition has been explained through the concept of magnetic anisotropy by Albrecht et al. [53]. These researchers stated that the magnetization within a ferromagnetic material ( $\mathbf{M}_T$ ) is uniform whereby its magnetic moments rotate in unison. The equation for  $\mathbf{M}_T$  is written as:

$$M_T = \frac{\mu}{V} \quad (4)$$

where  $\mu$  and  $V$  are the magnetic moment and volume of the magnetic track respectively. As the magnetic field lines exit through the magnet track, the magnitude of  $\mathbf{B}$  is reduced due to the enlarging of field lines at the extremities.

As previously mentioned, the cell separation in a MAP stage is related to the magnetic field gradient. To achieve desirable cell trajectory within the chamber, the  $y$ -component of the magnetic field gradient ( $|\nabla \cdot \mathbf{B}_y^2|$ ) within the chamber has to be evaluated. Its mathematical simulation result is presented in Figure 6a, whereby the gradient of the magnetic field was found to be higher at the region around the wall of the ferromagnetic track. In the process of further validating the result, a graph of  $|\nabla \cdot \mathbf{B}_y^2|$  was plotted across the microchannel. It is illustrated in Figure 6b. The representatives of the three cutlines are in accordance with those described in Figure 5a. From this graph,  $\nabla \mathbf{B}_y^2$  is found to gradually reduce towards the channel walls, which coordinates at  $x = 0$  and  $x = 0.75$ . Since the direction of cell movement is related to magnetic field gradient, the cells with high magnetic susceptibility such as RBCs are attracted toward the magnetic track and vice versa for other nucleated blood cells. In contrast to the single permanent magnet configuration (refer to Supplementary Section 5), the use of ferromagnetic track in the middle of the chamber generated a higher value of magnetic field gradient in the order of  $10 \text{ T/m}^2$ . Therefore, this configuration fulfils the magnetic force requirement to separate cells in our proposed MAP system.

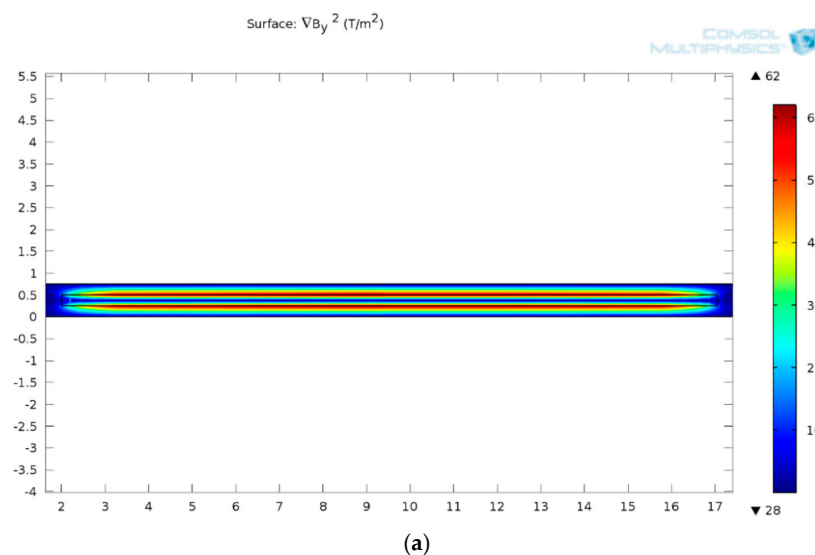
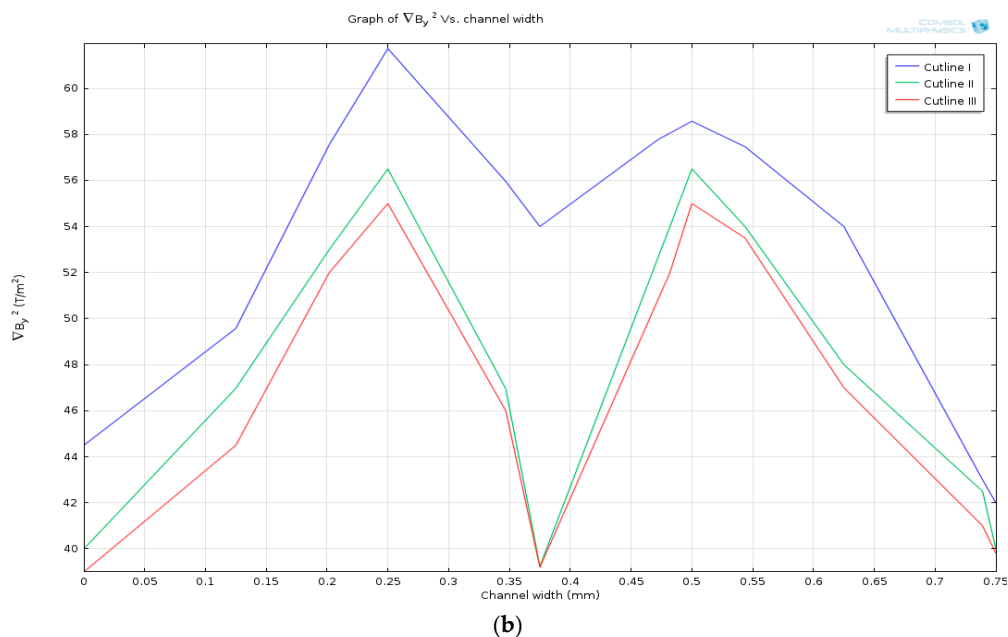


Figure 6. Cont.





**Figure 6.** Magnetic field gradient analysis: (a) Surface plot; (b) Graph of  $\nabla B_y^2$  across the channel width.

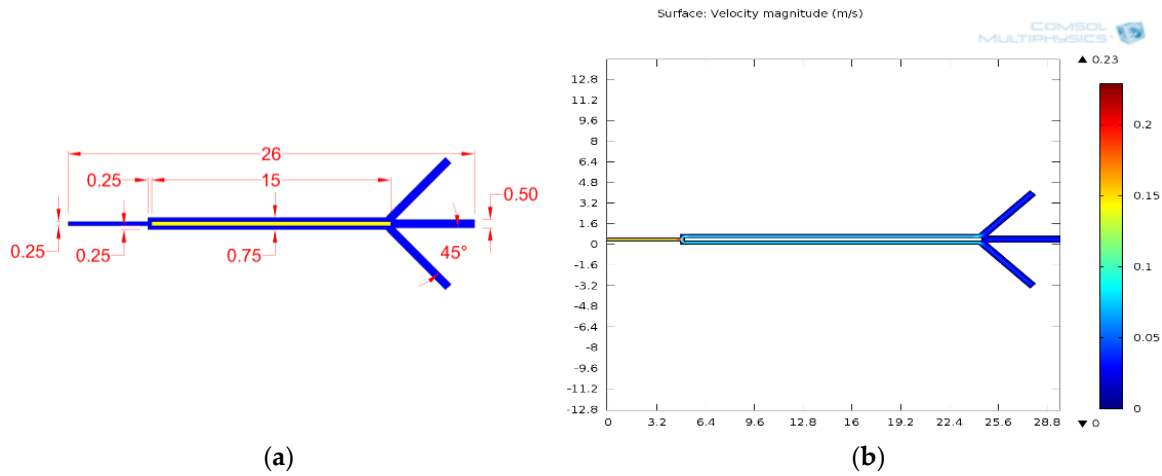
### 3.1.3. Fluid Flow Parameter and Dynamic Pressure of Proposed Microchannel

In a continuous cell sorting microfluidic system, the positioning of the ferromagnetic track in the middle of the microchannel can improve separation efficiency from two perspectives. Firstly, as the individual ferromagnetic piece, it will generate an extra short-ranged magnetic force within the microchannel to retain target cells (RBC) on its surface. Secondly, by acting as the flow divider, it directs cell suspension toward the bifurcation channel at both sides of the magnetic track, thus increasing the volumetric flow of blood sample exposed to MAP force per second.

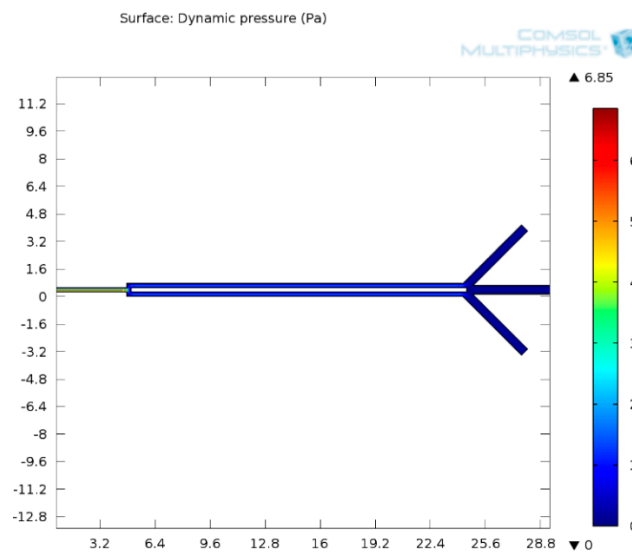
A devised schematic of the proposed microfluidic channel geometrical design for the MAP stage was illustrated in conjunction with the presence of the ferromagnetic track (see Figure 7a). The central outlet channel which directed RBC toward the collection port was fixed at 0.5 mm. This value was provided based on the effective range of the high magnetic field, which was 0.1 mm from the wall of the ferromagnetic track (see Figure 6b). According to Murray's Law, both cross section and shape of the drain channel at  $n$ -th level must be the same to equalize the hydraulic resistance within the outlet channels [54]. Therefore, the lateral outlet channel would have the same dimension as the central outlet. They were designated at an angle of  $45^\circ$  from the central outlet channel. Notably, both magnetic and hydrodynamic forces dominate cell motion within the MAP microchamber. To adapt the ferromagnetic track toward an effective continuous-flow cell separation, both flow velocity and dynamic pressure generated within our proposed microfluidic channel were examined. This was achieved with Navier-Stokes simulation. For the geometrical design as depicted in Figure 7a, the boundary condition of the inlet velocity is fixed at 0.18 m/s to fulfil the optimum flow velocity as stated in Supplementary Section 1.2. Its calculation can be found in the Supplementary materials.

Figure 7b presents the simulation result of the fluid flow velocity profile within our proposed channel. This surface plot indicates the velocity field in the colour spectrum. When blood sample was simulated to flow into the inlet, an acceleration meniscus was formed at the flow centre [55]. Such a condition caused the flow velocity within an inlet channel to be slightly higher than the specified inlet velocity. This was proved by a red spectral segment in this region which approximated to 0.02 m/s. As the flow was transported through the symmetrically-split-downstream channels, a downward colour sweep which indicated a decrease in the velocity field was observed in the surface plot. Such a condition is caused by the increase of hydraulic resistance within the proposed design and was explained in detail in our previous paper [56]. Interestingly, a study conducted by

Berthier et al. [57] showed that the hydraulic resistance within a microfluidic channel corresponds to the dynamic fluid pressure. To ensure continuity of the fluid flow, the dynamic fluid pressure generated within our proposed microchannel was evaluated. Its surface plot is shown in Figure 8.



**Figure 7.** (a) The proposed microfluidic channel architecture for MAP and (b) its surface velocity plot.



**Figure 8.** Surface plot of fluid dynamic pressure.

From this plot, the flow-driven pressure in the microchannel was found to decrease as the sample flows from the inlet toward the outlet. This phenomenon can be explained by rewriting the Navier-Stokes Equation analogously to Classical Ohm's law ( $V = RI$ ) [58]. In this context, a fluid pressure corresponds to an electrical voltage ( $p \sim V$ ); the volumetric flow rate corresponds to the electrical current ( $Q \sim I$ ) and flow resistance  $R_H$  corresponds to an electrical resistor,  $R$ . Thus the dynamic pressure drop generated within the microfluidic channel is equal to:

$$\Delta P = R_H Q \quad (5)$$

In this equation,  $\Delta P$  is directly proportional to  $R_H$  as  $Q$  is held constant. Therefore, the increase of  $R_H$  due to the presence of multiple sub-channels will develop a great  $\Delta P$ . Noteworthy,  $\Delta P$  in Figure 8 can be obtained by subtracting the outlet pressure ( $P_{out}$ ) from the inlet pressure ( $P_{in}$ ). As the dynamic pressure obtained at the outlet ( $P_{out}$ ) of our proposed microfluidic design was approximate to  $\sim 0$  Pa,

$\Delta P$  would have a similar value to  $P_{in}$ . However, such a condition is undesirable as it results in cells not having sufficient kinetic momentum to move toward the DEP stage. To circumvent this problem,  $P_{out}$  needs to be increased. It can be accomplished by reducing the total hydraulic resistance impact on the microfluidic system.

According to Hagen-Poiseuille Law, the theoretical fluidic resistance  $R_H$  within each channel can be determined using geometric parameters, through the summation of a Fourier series, as in Equation (6) below:

$$R_H = \frac{12\mu \cdot L}{wh^3 \left( 1 - 0.63 \frac{h}{w} \left( \sum_{n=1}^{\infty} \frac{1}{n^5} \tanh \left( 1.57 \frac{w}{h} \right) \right) \right)} \quad (6)$$

where  $h$  represents a channel cross sections height,  $L$  is the channel cross section length, while  $w$  refers to the width. Since the aspect ratio (depth/width) of inlet and outlet is approximate to 1 and 2 respectively, the hydraulic resistance of the channel for our design can be generalized as:

$$R_H = \begin{cases} \frac{12\mu L}{wh^3}, & \frac{h}{w} = 1 \text{ (e.g., outlet channels)} \\ \frac{600\mu L}{29wh^3}, & \frac{h}{w} = 2 \text{ (e.g., inlet channel and bifurcated channels along the track)} \end{cases} \quad (7)$$

This equation shows  $R_H$  is inversely proportional to  $w$  and  $h$ , and vice versa for  $L$ . Since both length and height remain constant for each sub-channel, the calculation of  $R_H$  is dependent on the channel width. As discussed earlier in this section, the width for both outlet channel and sub-channel along a ferromagnetic track were fixed to  $500 \mu\text{m}$  and  $250 \mu\text{m}$  respectively in order to enhance the magnetic force exacted on the cells. Therefore,  $R_H$  within the proposed design was reduced by increasing the inlet channel width. The updated microfluidic design is depicted in Figure 9a.

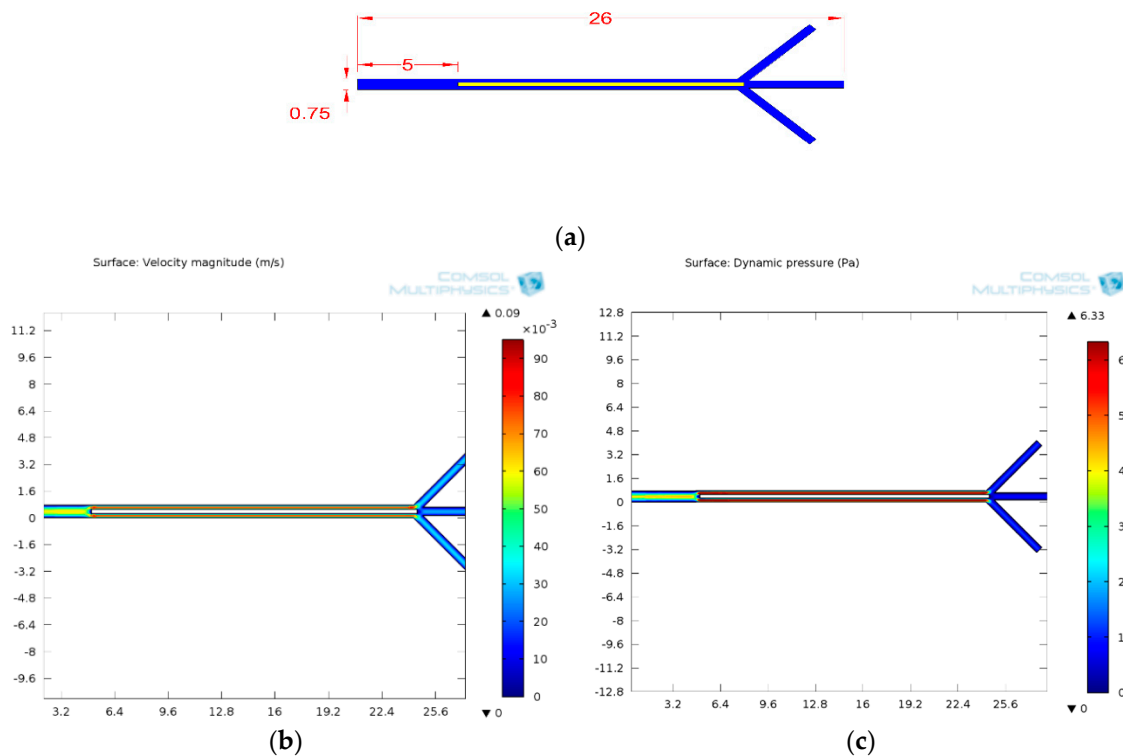


**Figure 9.** (a) The updated design for our proposed MAP stage and its surface plot of (b) velocity field and (c) fluid dynamic pressure.

To test the effectiveness of width alteration on both the velocity and the dynamic pressure profile, the improvised microfluidic architecture was examined with COMSOL software. Due to a change in the inlet width, there was a need to adjust the inlet velocity ( $V_{in}$ ) in order to meet the flow velocity

requirement within the MAP chamber. Using the classical rule explained in the Supplementary Information, the velocity of the inlet boundary condition was fixed at 60 mm/s. The surface plots of the velocity field and fluid dynamic pressure are presented in Figure 9b,c, respectively.

From Figure 9c, it can be deduced that increasing width coupled with a decrease of inlet boundary velocity resulted in the inlet dynamic pressure being lower than in the previous design. When the fluid flows from a wide to a narrow channel, the dynamic pressure is increased corresponding to the increase of flow velocity. As the blood sample travels toward the outlet channel, a transition from the velocity profile at the entrance to multiple outlets results in a drop in  $P_{out}$ . A  $P_{out}$  of 0.5 Pa was obtained in the improvised design (see Figure 9c). To enhance the cellular kinetic motion, 0.75 mm was therefore adopted as the inlet width value.

### 3.1.4. Design Optimization

Although the rectangular cross-sectional microfluidic channel design is easy to fabricate, two drawbacks were discovered. Firstly, as alluded in Section 3.1.2, an extremely high magnetic field region was found at the sharp edge of the ferromagnetic track; secondly, when a continuous flow was subjected to the channel, multiple-zero-velocity areas were detected in the sharp corners. Both of these issues can be further evidenced through simulation results as presented in Figure 10. A bright cyan colour segment at the edge of the inbuilt ferromagnetic track in Figure 10a represents high magnetic field. Meanwhile the dark blue colour segment around the sharp corner in Figure 10b represents a zero velocity profile. This situation causes a large number of cells to accumulate around a sharp corner region. Because of this, the sharp turns or edges are therefore not optimal for cell separation application.

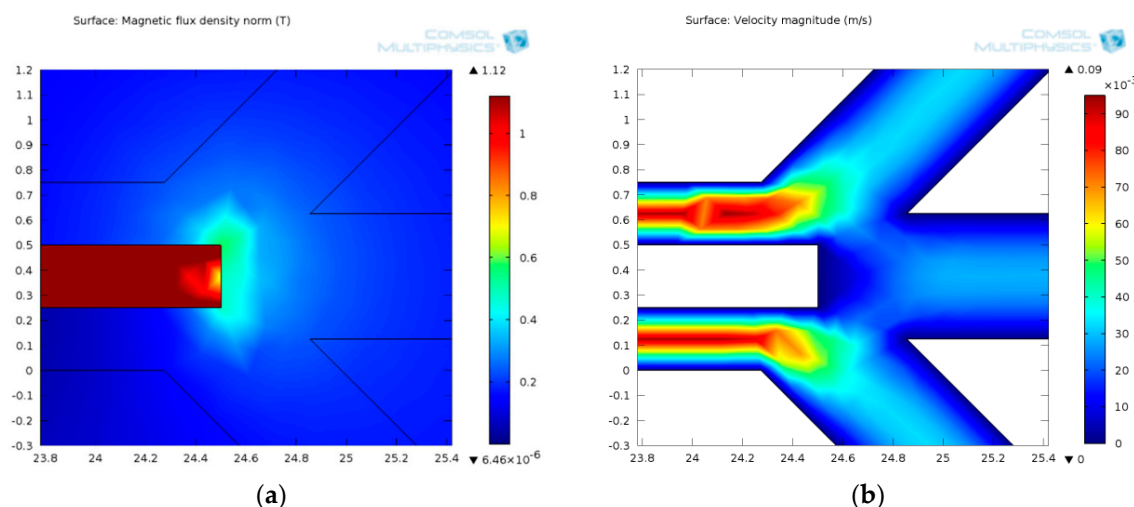


**Figure 10.** Surface plots: (a) Magnetic field and (b) velocity field at the sharp corner of the microfluidic channel.

According to studies conducted by both Feng et al. [59] and Green et al. [60], a round-shaped turn was identified to generate uniform velocity profiles and cell adhesion within the channel. Thus, the sequence of round-shape turns was used to replace the sharp corner of our original proposed microfluidic channel architecture. The optimized geometrical design is presented in Figure 11a.

The channel geometrical design was then re-examined with COMSOL software. In contrast to previous design in this study, the surface plots indicate a reduction of high magnetic field (Figure 11b) and zero velocity field (Figure 11c) region at the rounded surface of the ferromagnetic track. It can be further described through the comparison graph plotted with MATLAB as illustrated in Figure 12.

In Figure 12a, the magnetic field generated at the edge of the ferromagnetic track is observed to be reduced in the rounded edge in contrast to the sharp corner. This reduction can be explained by the

fact that the rounding suppresses the pinning fields in the vicinity of the sharp corner [61]. Meanwhile, when the velocity field was measured across the width of our proposed MAP microchamber (see Figure 12b), both models showed a reduction in velocity field at the region next to the bifurcated channel wall. Such a condition is caused by the generation of shear stress which acts on the wall surface in the direction of fluid flow. However, comparing to our original design with the presence of sharp corners, a uniform velocity profile is presented within the improved architecture (at distances between 0 to 0.25 mm and 0.5 to 0.75 mm). Such a profile is thereby encouraging homogenous cell adhesion within it. Due to the improvement in magnetic and velocity fields shown by this design, the improvised geometry was employed as the design to be used in our MAP platform.

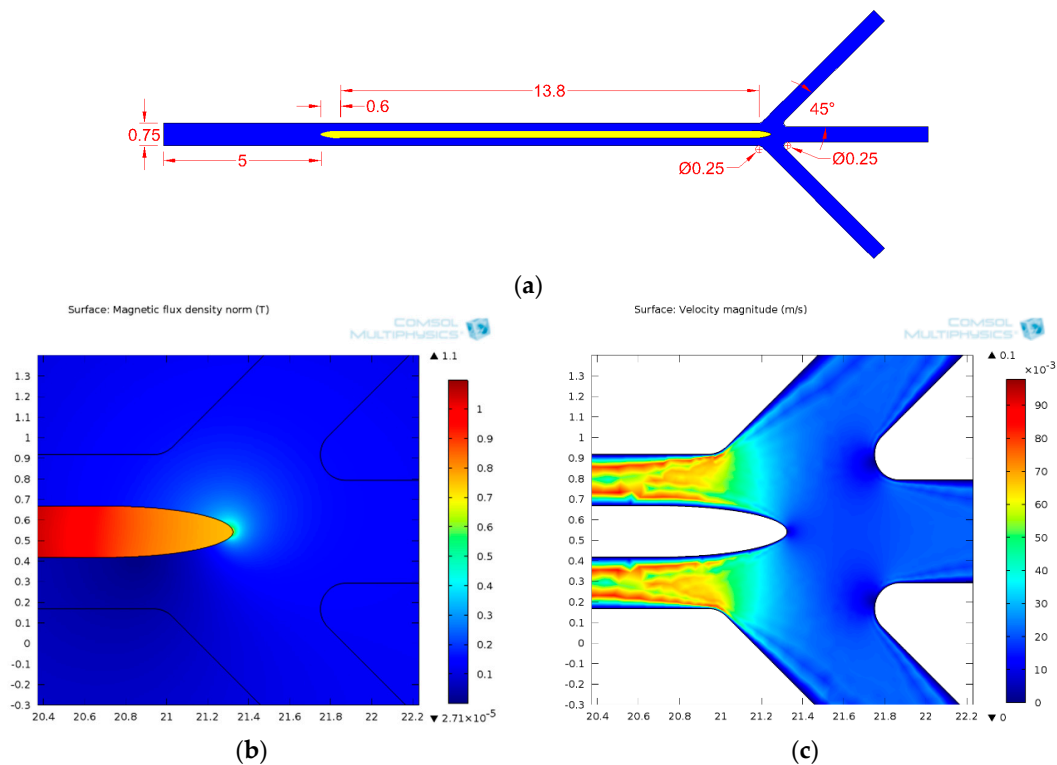


**Figure 11.** (a) Schematic of microfluidic channel layout with rounded corner. The surface plot of the magnetic and velocity field at the optimized ferromagnetic edge region is presented in (b,c), respectively.

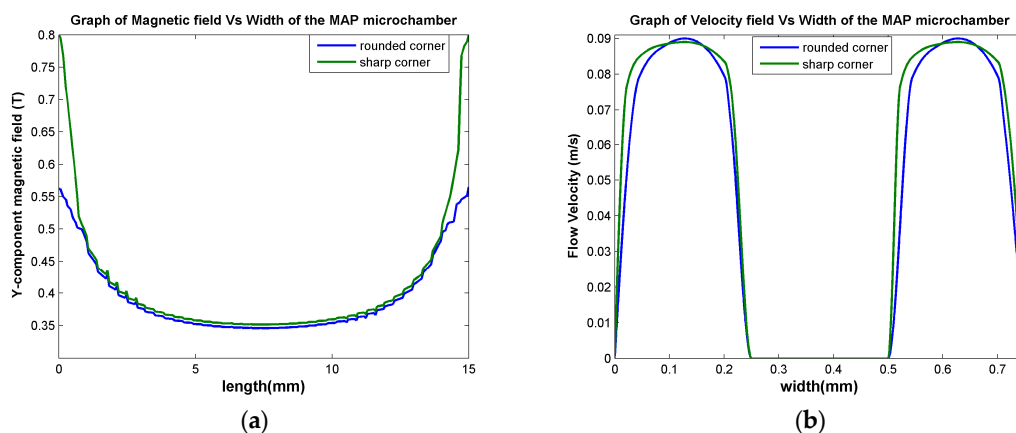


**Figure 12.** Graph of comparison for rounded and sharp corner: (a) Y-component magnetic field across the middle of the ferromagnetic track; (b) Average velocity field across the width of the MAP microchamber.



### 3.1.5. Separation Efficiency

For our proposed MAP device architecture, the particle motion within it can be observed via a particle tracing module, whereby cell trajectory plots for RBC and other nucleated blood cells in the presence of MAP is respectively illustrated in Figure 13a,b. To visualize the cell motion more easily, the particles were coloured according to their magnetic susceptibilities.

As evidenced in Figure 13a, the presence of the MAP force allows RBCs (red-colour-labelled particle) to be attracted toward the ferromagnetic track surface and vice versa for other cells (see Figure 13b). Such a condition can be explained through the graph in Figure 13c. In the plotted graph, RBCs were found to exhibit positive MAP force and vice versa for the other cells. The difference in sign indicated that the forces exerted on cells are in opposite directions. However, there is a magnitude variation among these cell types. For example, the MAP force subjected on the breast cancer cell was stronger in contrast to other cells. Such a condition is caused by the difference in cell volume (see Equation (2)). When the calculated MAP force is compared to the calculated lift force, the lift force shows a lower order of magnitude for the analysed cell types. Under this distribution, a MAP force is dominant across the microchannel and the lift force cannot disrupt the lateral motion of cells across the channel.

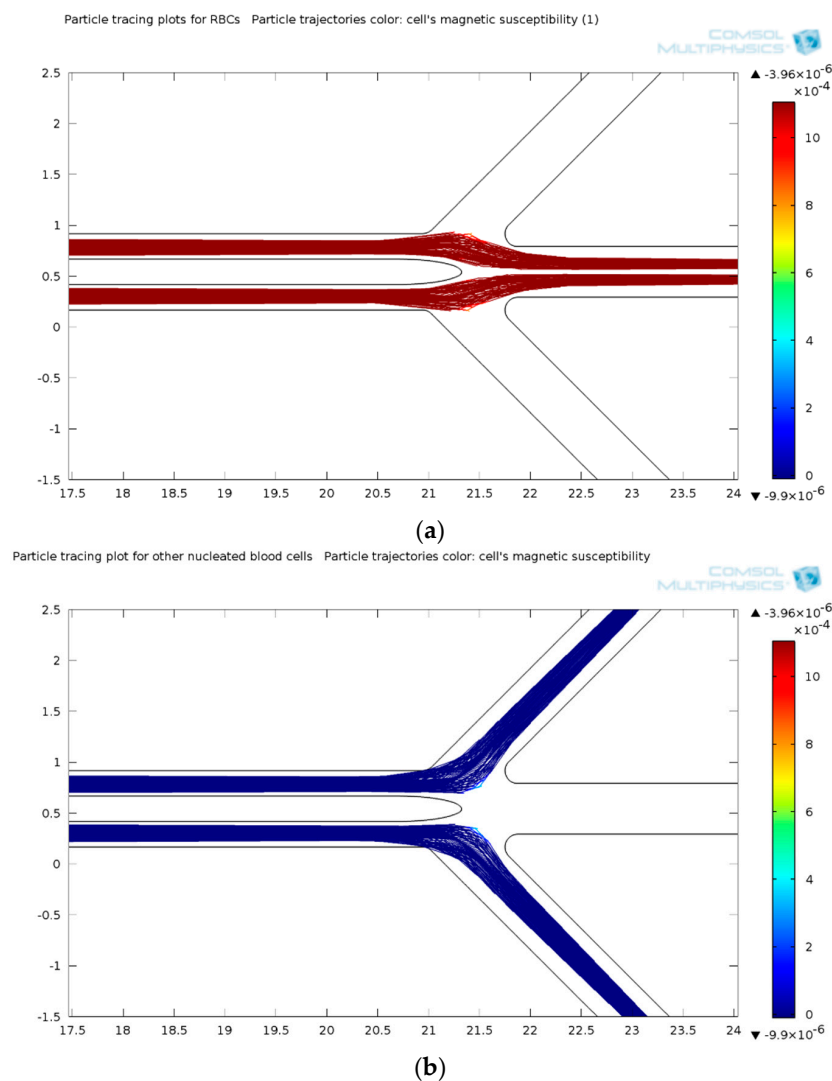
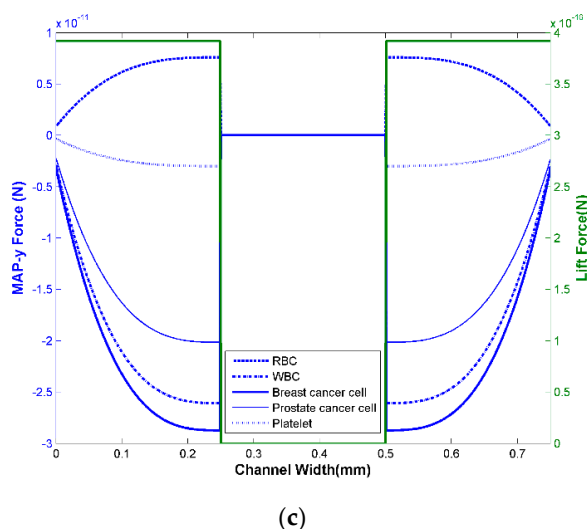
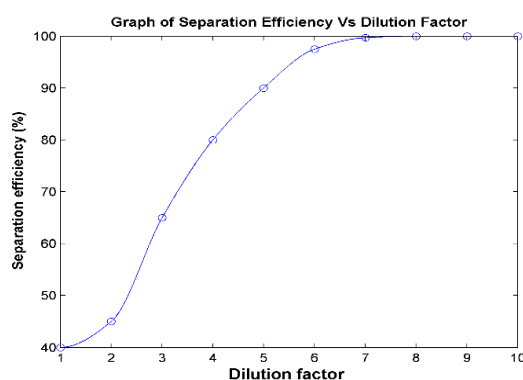


Figure 13. Cont.



**Figure 13.** Plot of cell trajectories in the presence of MAP for (a) RBCs and (b) other nucleated blood cells (WBCs, platelets, and CTCs). The colour spectrum bar indicates the magnetic susceptibilities of cells, as such RBCs are represented by red particles while other nucleated cells are blue. The cell motion was explained through the graph of calculated y-directional magnetic and hydrodynamic forces as illustrated in (c). Zero forces were found in the region bounded by  $x = 0.25$  and  $x = 0.5$  due to the presence of inbuilt ferromagnetic track, which was simulated to have the same height as the microchannel.

Notably, separation efficiency is the ultimate performance evaluation of our proposed MAP microchamber design. However, it was shown that the concentration of cells carried by the fluid flow affect the number of cells to be delivered into a designated outlet under a constant velocity [62]. Such a condition will indirectly affect the recovery rate of the proposed device. To enhance the performance of the MAP stage, the separation efficiencies for various dilution ratios as discussed in Supplementary Section 2.5 were studied. For the purpose of reducing both RAM memory usage and computation time, the simulation was performed with 1 mL blood sample. As stated in the introduction, the presences of tumour cells are rare in a blood sample, of the order of 1–10 per 7.5 mL. Furthermore, it has been shown by previous results whereby tumour cells exhibited a similar response to WBC in the MAP stage. Considering the purpose of the MAP stage was to separate RBC from blood sample, the tumour cells were neglected in this simulation. Notably, the central outlet serves as collection port for targeted cells (RBC) in the MAP stage. Therefore, the simulated separation efficiency ( $\eta$ ) can be calculated directly based on the ratio of RBC obtained in the central outlet to the total amount of RBC injected at the inlet. A plot of separation efficiency versus dilution factor (ratio of final volume/aliquot volume) is illustrated in Figure 14.



**Figure 14.** Graph of separation efficiency vs. dilution ratio in the MAP stage.

From the graph, the separation efficiency for dilution ratios of 1:0, 1:2, and 1:3 is considerably low, whereby the calculated value ranges from 40 to 65. Such a condition is in agreement with a study conducted by Guldiken et al. [63] which stated that the high concentration of cells impedes the separation process within microfluidic devices. Interestingly, the separation efficiency is found to be enhanced with an increase of dilution ratio. A 100% recovery rate was obtained when the blood samples with dilution ratios of 1:7, 1:8, 1:9, and 1:10 were simulated in our proposed device. Note that a high dilution ratio will lower the throughput in contrast to the low-dilution ratio sample. To enhance the separation efficiency without compromising the device throughput, the sample with dilution ratio of 1:7 was selected to compute the evaluation of the whole integrated platform in the next section.

### 3.2. Evaluation with DEP Stage

The previous section showed the proposed MAP stage to be able to separate RBC from other nucleated cells with high efficiency. As the enriched nucleated cells undergo a second separation at the downstream DEP stage, it was crucial for us to investigate the final isolation performance in this cooperative platform. A planar electrode developed by Moon et al., (2011) was adopted and integrated with our proposed MAP platform for the purpose of evaluation. These electrodes were placed at the bottom of the microchannel with an angle of  $30^\circ$  to the direction of flow. Both width and spacing of the interdigitated electrodes were  $250\text{ }\mu\text{m}$ . To initiate DEP separation, the electrode arrays were connected to 1 MHz and  $15\text{ V}_{\text{p-p}}$  sinusoidal voltages. From a theoretical perspective, an interdigitated electrode array with an applied voltage can be modelled more simply as line charges placed on the edges of the electrode. As such, an electrode array coloured with green and blue is connected to a positive or negative voltage terminal, respectively.

In order to achieve a uniform loading capacity for a given chamber size, a tree-network design from our previous study [56] was implemented into the geometrical design in this DEP stage. It refers to the branched channel geometry in between both MAP and DEP stages. The inspiration of this design is from the tubular network of blood vessels in the human body, in which the presence of bifurcation topology in the design is able to generate hydraulic resistance within the channel. For this particular design, the cross section and the length of a drain channel are the same as the outlet channel of the MAP stage. This is to help in equalizing the hydraulic resistance within these channels and thereby generating a uniform flow distribution throughout the whole wide chamber of the DEP stage. Such a condition has been defined theoretically in Low et al. [56]. To reduce the presence of a zero velocity within channels, a curved corner as discussed in the previous section was employed. The overall integrated MAP-DEP platform is illustrated in Figure 15a. As shown in this figure, the length of the DEP microchamber was fixed at 15 mm. Meanwhile, the microchamber width was 3.5 mm which was determined based on the summation of the drain channel's widths.

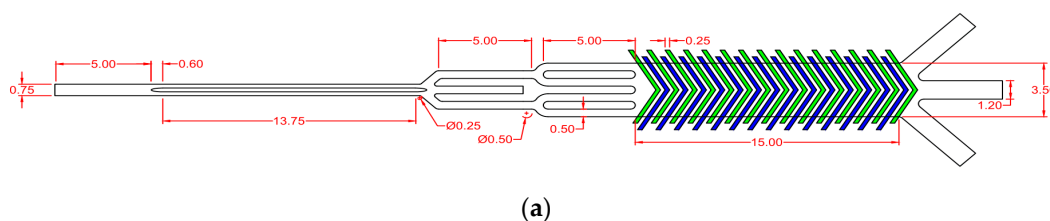
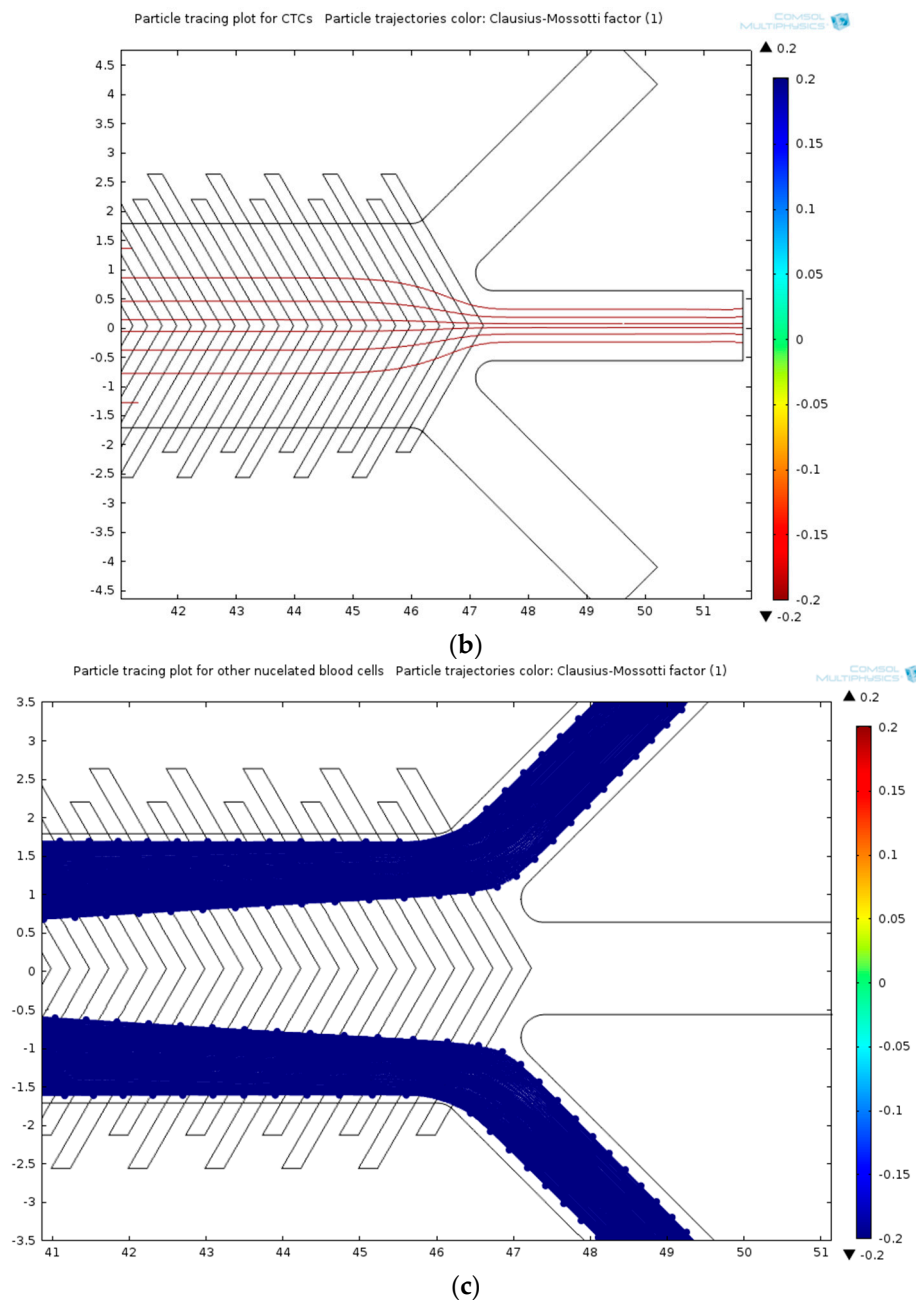


Figure 15. Cont.



**Figure 15.** (a) Schematic of the microchannel architecture of integrated MAP-DEP microsystem. When cells isolated from the MAP stage are directed toward the DEP stage, the trajectories of nucleated cells such as WBC (and platelet) and CTCs are displayed in (b,c), respectively. The spectrum bar indicates the Clausius-Mossotti factor of the cells.

When a concentrated nucleated cell from our proposed MAP stage is directed into the DEP stage, the movement of the cell passing onto these interdigitated electrode arrays is illustrated in Figure 15b,c. In this case, a CTC was found to manifest an opposite response in contrast to other nucleated cells. Notably, the middle part of this DEP stage consists of a high electric field region. As the CTCs exhibit pDEP (CM factor  $>0$ ), it deviates toward this region and flows into the central outlet. On the contrary, nDEP force (CM factor  $<0$ ) pushes the normal nucleated cell toward the low electric field region along the channel wall. Under hydrodynamic force, these cells flow into the lateral outlet. Comparing to a previous study as discussed in literature [19,28], there is an improvement in

throughput and separation efficiency shown by this device. Therefore, a MAP stage should be adopted as a new integrated technique to be cooperated in a DEP system.

#### 4. Conclusions and Future Works

Overall, the present work set out with the objective to solve the limitation of dielectrophoresis (DEP) technique in CTC isolation. The general strategy of achieving this aim was by developing a magnetophoresis (MAP) system as a pre-enrichment stage. Using this strategy, red blood cells are first removed from the blood sample in the MAP stage, thus allowing the DEP stage to focus on isolation of targeted rare cells. Several computational models were employed to demonstrate the proof-of-concept of our proposed method for enhancing the device separation efficiency. These models combined an Eulerian-Lagrangian CFD analysis with a closed-form magnetic field analysis to predict cell separation, taking into account dominant magnetic and hydrodynamic forces. There were a few unique features of these elements that contributed to the proposed device's capture performance. First, a single permanent magnet was employed to produce a region of both attractive and repulsive magnetic forces within the MAP stage. In order to amplify low magnetic forces on blood cells, a ferromagnetic track was embedded in the middle of the MAP microchamber. This strategy generated a higher value of magnetic field gradient in the order of  $10 \text{ T/m}^2$ . Besides, from the perspective of Navier-Stokes principle, the positioning of the ferromagnetic track in the middle of the microchannel created a hydraulic resistance within the bifurcated channel, thus resulting in a uniform flow velocity. Last but not least, a tree-network division was implemented onto the platform design to generate uniform cell distribution across the microchamber.

In short, this cooperative platform utilising integrated separation modalities reduced the overloading cell issues within the DEP stage, thus the enhanced capture. Furthermore, the computational model which was portrayed in this paper has offered a rational design of systems in advance of fabrication and should be of considerable interest to researchers in the future development of lab-on-chip systems. At the moment, the proposed microfluidic design was solely based on numerical analysis. However, this simulation might not reflect the real condition during the experimental platform analysis. For instance, errors which occur during the fabrication process of the microfluidic channel will influence cell motion, thus affecting their distribution within the microfluidic chamber. Furthermore, storage-related activity deterioration of blood components might occur during the actual experiment and affect the device's efficiency. These conditions have not been considered in our simulation due to the limited precision of data for cells which have high conductivity or closer bonding. Therefore, there is a need for experimental characterization to verify the design strategy and simulation. A brief discussion for future experimental setup and device fabrication is included in the Supplementary Information.

**Supplementary Materials:** The following are available online at [www.mdpi.com/2227-9040/4/3/14/s1](http://www.mdpi.com/2227-9040/4/3/14/s1).

**Acknowledgments:** This study was financially supported by the University of Malaya Research Grant (RG156-12AET).

**Author Contributions:** In this paper, Wan Shi Low conducted simulation and prepared the draft manuscript. Nahrizul Adib Kadri conducted the analysis and proofed the manuscript

**Conflicts of Interest:** The authors declare no conflict of interest.

#### References

1. Maryam, F.; Hassali, M.A.; Knight, A.; Shafie, A.A.; Farooqui, M.A.; Saleem, F. A qualitative exploration of malaysian cancer patients' perceptions of cancer screening. *BMC Public Health* **2013**, *13*, 1–7.
2. Thiery, J.P. Epithelial-mesenchymal transitions in tumour progression. *Nat. Rev. Cancer* **2002**, *2*, 442–454. [[CrossRef](#)] [[PubMed](#)]
3. Frangioni, J.V. New technologies for human cancer imaging. *J. Clin. Oncol.* **2008**, *26*, 4012–4021. [[CrossRef](#)] [[PubMed](#)]



4. Husemann, Y.; Geigl, J.B.; Schubert, F.; Musiani, P.; Meyer, M.; Burghart, E.; Forni, G.; Eils, R.; Fehm, T.; Riethmuller, G.; et al. Systemic spread is an early step in breast cancer. *Cancer Cell* **2008**, *13*, 58–68. [[CrossRef](#)] [[PubMed](#)]
5. Gerges, N.; Rak, J.; Jabado, N. New technologies for the detection of circulating tumour cells. *Br. Med. Bull.* **2010**, *94*, 49–64. [[CrossRef](#)] [[PubMed](#)]
6. Allen, J.E.; El-Deiry, W.S. Circulating tumor cells and colorectal cancer. *Curr. Colorectal Cancer Rep.* **2010**, *6*, 212–220. [[CrossRef](#)] [[PubMed](#)]
7. Dalum, G.V.; Holland, L.; Terstappen, L.W. Metastasis and circulating tumor cells. *J. Int. Fed. Clin. Chem. Lab. Med.* **2012**, *23*, 1–11.
8. Michaelson, J.S.; Cheongsiatmoy, J.A.; Dewey, F.; Silverstein, M.J.; Sgroi, D.; Smith, B.; Tanabe, K.K. Spread of human cancer cells occurs with probabilities indicative of a nongenetic mechanism. *Br. J. Cancer* **2005**, *93*, 1244–1249. [[CrossRef](#)] [[PubMed](#)]
9. Antolovic, D.; Galindo, L.; Carstens, A.; Rahbari, N.; Buchler, M.W.; Weitz, J.; Koch, M. Heterogeneous detection of circulating tumor cells in patients with colorectal cancer by immunomagnetic enrichment using different epcam-specific antibodies. *BMC Biotechnol.* **2010**, *10*, 35. [[CrossRef](#)] [[PubMed](#)]
10. Khoo, B.L.; Chaudhuri, P.K.; Ramalingam, N.; Tan, D.S.; Lim, C.T.; Warkiani, M.E. Single-cell profiling approaches to probing tumor heterogeneity. *Int. J. Cancer* **2016**, *139*, 243–255. [[CrossRef](#)] [[PubMed](#)]
11. Kallergi, G.; Papadaki, M.A.; Politaki, E.; Mavroudis, D.; Georgoulas, V.; Agelaki, S. Epithelial to mesenchymal transition markers expressed in circulating tumour cells of early and metastatic breast cancer patients. *Breast Cancer Res.* **2011**, *13*, 1–11. [[CrossRef](#)] [[PubMed](#)]
12. Marrinucci, D.; Bethel, K.; Lazar, D.; Fisher, J.; Huynh, E.; Clark, P.; Bruce, R.; Nieva, J.; Kuhn, P. Cytomorphology of circulating colorectal tumor cells: A small case series. *J. Oncol.* **2010**, *2010*. [[CrossRef](#)] [[PubMed](#)]
13. Cima, I.; Wen Yee, C.; Iliescu, F.S.; Min Phy, W.; Hon Lim, K.; Iliescu, C.; Han Tan, M. Label-free isolation of circulating tumor cells in microfluidic devices: Current research and perspectives. *Biomicrofluidics* **2013**, *7*. [[CrossRef](#)] [[PubMed](#)]
14. Zheng, S.; Lin, H.K.; Lu, B.; Williams, A.; Datar, R.; Cote, R.J.; Tai, Y.C. 3D microfilter device for viable circulating tumor cell (CTC) enrichment from blood. *Biomed. Microdevices* **2011**, *13*, 203–213. [[CrossRef](#)] [[PubMed](#)]
15. Coumans, F.A.; van Dalum, G.; Beck, M.; Terstappen, L.W. Filter characteristics influencing circulating tumor cell enrichment from whole blood. *PLoS ONE* **2013**, *8*, e61770. [[CrossRef](#)] [[PubMed](#)]
16. Sun, J.; Liu, C.; Li, M.; Wang, J.; Xianyu, Y.; Hu, G.; Jiang, X. Size-based hydrodynamic rare tumor cell separation in curved microfluidic channels. *Biomicrofluidics* **2013**, *7*. [[CrossRef](#)] [[PubMed](#)]
17. Warkiani, M.E.; Guan, G.; Luan, K.B.; Lee, W.C.; Bhagat, A.A.S.; Kant Chaudhuri, P.; Tan, D.S.-W.; Lim, W.T.; Lee, S.C.; Chen, P.C.Y.; et al. Slanted spiral microfluidics for the ultra-fast, label-free isolation of circulating tumor cells. *Lab Chip* **2014**, *14*, 128–137. [[CrossRef](#)] [[PubMed](#)]
18. Huang, C.-T.; Amstislavskaya, T.G.; Chen, G.-H.; Chang, H.-H.; Chen, Y.-H.; Jen, C.-P. Selectively concentrating cervical carcinoma cells from rare blood cells utilizing dielectrophoresis with circular ito electrodes in stepping electric fields. *J. Med. Biol. Eng.* **2012**, *33*, 51–59. [[CrossRef](#)]
19. Moon, H.S.; Kwon, K.; Kim, S.I.; Han, H.; Sohn, J.; Lee, S.; Jung, H.I. Continuous separation of breast cancer cells from blood samples using multi-orifice flow fractionation (moff) and dielectrophoresis (dep). *Lab Chip* **2011**, *11*, 1118–1125. [[CrossRef](#)] [[PubMed](#)]
20. Park, S.; Ang, R.R.; Duffy, S.P.; Bazov, J.; Chi, K.N.; Black, P.C.; Ma, H. Morphological differences between circulating tumor cells from prostate cancer patients and cultured prostate cancer cells. *PLoS ONE* **2014**, *9*, e85264. [[CrossRef](#)] [[PubMed](#)]
21. Mulhall, H.J.; Labeed, F.H.; Kazmi, B.; Costea, D.E.; Hughes, M.P.; Lewis, M.P. Cancer, pre-cancer and normal oral cells distinguished by dielectrophoresis. *Anal. Bioanal. Chem.* **2011**, *401*, 2455–2463. [[CrossRef](#)] [[PubMed](#)]
22. Broche, L.M.; Bhadal, N.; Lewis, M.P.; Porter, S.; Hughes, M.P.; Labeed, F.H. Early detection of oral cancer—Is dielectrophoresis the answer? *Oral Oncol.* **2007**, *43*, 199–203. [[CrossRef](#)] [[PubMed](#)]
23. Fabbri, F.; Carloni, S.; Zoli, W.; Ulivi, P.; Gallerani, G.; Fici, P.; Chiadini, E.; Passardi, A.; Frassinetti, G.L.; Ragazzini, A.; et al. Detection and recovery of circulating colon cancer cells using a dielectrophoresis-based device: Kras mutation status in pure CTCs. *Cancer Lett.* **2013**, *335*, 225–231. [[CrossRef](#)] [[PubMed](#)]

24. Huang, C.; Liu, H.; Bander, N.H.; Kirby, B.J. Enrichment of prostate cancer cells from blood cells with a hybrid dielectrophoresis and immunocapture microfluidic system. *Biomed. Microdevices* **2013**, *15*, 941–948. [[CrossRef](#)] [[PubMed](#)]
25. Vykoukal, D.M.; Gascoyne, P.R.; Vykoukal, J. Dielectric characterization of complete mononuclear and polymorphonuclear blood cell subpopulations for label-free discrimination. *Integr. Biol.* **2009**, *1*, 477–484. [[CrossRef](#)] [[PubMed](#)]
26. Leu, T.-S.; Liao, Z.-F. Separating plasma and blood cells by dielectrophoresis in microfluidic chips. *Int. J. Mod. Phys. Conf. Ser.* **2012**, *19*, 185–189. [[CrossRef](#)]
27. Toner, M.; Irimia, D. Blood-on-a-chip. *Annu. Rev. Biomed. Eng.* **2008**, *7*, 77–103. [[CrossRef](#)] [[PubMed](#)]
28. Gascoyne, P.R.C.; Noshari, J.; Anderson, T.J.; Becker, F.F. Isolation of rare cells from cell mixtures by dielectrophoresis. *Electrophoresis* **2009**, *30*, 1388–1398. [[CrossRef](#)] [[PubMed](#)]
29. Shim, S.; Gascoyne, P.; Noshari, J.; Hale, K.S. Dynamic physical properties of dissociated tumor cells revealed by dielectrophoretic field-flow fractionation. *Integr. Biol.* **2011**, *3*, 850–862. [[CrossRef](#)] [[PubMed](#)]
30. Gupta, V.; Jafferji, I.; Garza, M.; Melnikova, V.O.; Hasegawa, D.K.; Pethig, R.; Davis, D.W. Apostream<sup>TM</sup>, a new dielectrophoretic device for antibody independent isolation and recovery of viable cancer cells from blood. *Biomicrofluidics* **2012**, *6*. [[CrossRef](#)] [[PubMed](#)]
31. Wang, L.H.; Lawrence, S.M.; Navas, T.; Kinderss, R.J. Characterization of CTCs from peripheral blood specimens of patients (using aposteam instruments). In *American Society of Clinical Oncology Annual Meeting 2014*; American Society of Clinical Oncology: Chicago, IL, USA, 2014.
32. Gascoyne, P.R.C.; Shim, S. Isolation of circulating tumor cells by dielectrophoresis. *Cancers* **2014**, *6*, 545–579. [[CrossRef](#)] [[PubMed](#)]
33. Pommer, M.S.; Zhang, Y.; Keerthi, N.; Chen, D.; Thomson, J.A.; Meinhart, C.D.; Soh, H.T. Dielectrophoretic separation of platelets from diluted whole blood in microfluidic channels. *Electrophoresis* **2008**, *29*, 1213–1218. [[CrossRef](#)] [[PubMed](#)]
34. Liao, S.H.; Chang, C.Y.; Chang, H.C. A capillary dielectrophoretic chip for real-time blood cell separation from a drop of whole blood. *Biomicrofluidics* **2013**, *7*. [[CrossRef](#)] [[PubMed](#)]
35. Takaori, M. Changes of pH of blood diluted with plasma and plasma substitutes in vitro. *Transfusion* **1966**, *6*, 597–599. [[CrossRef](#)] [[PubMed](#)]
36. Lynch, E.C. Peripheral blood smear. In *Clinical Methods: The History, Physical, and Laboratory Examinations*; Walker, H.K., Hall, W.D., Hurst, J.W., Eds.; Butterworths: Boston, MA, USA, 1990.
37. Gassner, A.L.; Abonnenc, M.; Chen, H.X.; Morandini, J.; Josseland, J.; Rossier, J.S.; Busnel, J.M.; Girault, H.H. Magnetic forces produced by rectangular permanent magnets in static microsystems. *Lab Chip* **2009**, *9*, 2356–2363. [[CrossRef](#)] [[PubMed](#)]
38. Tomlinson, M.J.; Tomlinson, S.; Yang, X.B.; Kirkham, J. Cell separation: Terminology and practical considerations. *J. Tissue Eng.* **2013**, *4*. [[CrossRef](#)] [[PubMed](#)]
39. Essakali, S.; Carney, D.; Westerman, D.; Gambell, P.; Seymour, J.F.; Dobrovic, A. Negative selection of chronic lymphocytic leukaemia cells using a bifunctional rosette-based antibody cocktail. *BMC Biotechnol.* **2008**, *8*, 1–5. [[CrossRef](#)] [[PubMed](#)]
40. Esmaeilabzali, H.; Beischlag, T.V.; Cox, M.E.; Parameswaran, A.M.; Park, E.J. Detection and isolation of circulating tumor cells: Principles and methods. *Biotechnol. Adv.* **2013**, *31*, 1063–1084. [[CrossRef](#)] [[PubMed](#)]
41. Iliescu, C.; Xu, G.; Barbarini, E.; Avram, M.; Avram, A. Microfluidic device for continuous magnetophoretic separation of white blood cells. *Microsyst. Technol.* **2008**, *15*, 1157–1162. [[CrossRef](#)]
42. Shen, F.; Hwang, H.; Hahn, Y.K.; Park, J.-K. Label-free cell separation using a tunable magnetophoretic repulsion force. *Anal. Chem.* **2012**, *84*, 3075–3081. [[CrossRef](#)] [[PubMed](#)]
43. Jung, J.; Han, K.-H. Lateral-driven continuous magnetophoretic separation of blood cells. *Appl. Phys. Lett.* **2008**, *93*. [[CrossRef](#)]
44. Chen, J.; Abdelgawad, M.; Yu, L.; Shakiba, N.; Chien, W.-Y.; Lu, Z.; Geddie, W.R.; Jewett, M.A.S.; Sun, Y. Electrodeformation for single cell mechanical characterization. *J. Micromech. Microeng.* **2011**, *21*. [[CrossRef](#)]
45. Furiani, E.P. Magnetophoretic separation of blood cells at microscale. *J. Appl. Phys.* **2007**, *40*, 1313.
46. Baccelli, I.; Schneeweiss, A.; Riethdorf, S.; Stenzinger, A.; Schillert, A.; Vogel, V.; Klein, C.; Saini, M.; Bauerle, T.; Wallwiener, M.; et al. Identification of a population of blood circulating tumor cells from breast cancer patients that initiates metastasis in a xenograft assay. *Nat. Biotechnol.* **2013**, *31*, 539–544. [[CrossRef](#)] [[PubMed](#)]

47. Krawczyk, N.; Banys, M.; Hartkopf, A.; Hagenbeck, C.; Melcher, C.; Fehm, T. Circulating tumour cells in breast cancer. *Ecancermedicalscience* **2013**, *7*, 352. [[PubMed](#)]
48. Furtado, P.; Lima, M.V.A.; Nogueira, C.; Franco, M.; Tavora, F. Review of small cell carcinomas of the prostate. *Prostate Cancer* **2011**, 2011. [[CrossRef](#)] [[PubMed](#)]
49. Newton, M.R.; Phillips, S.; Chang, S.S.; Clark, P.E.; Cookson, M.S.; Davis, R.; Fowke, J.H.; Herrell, S.D.; Baumgartner, R.; Chan, R.; et al. Smaller prostate size predicts high grade prostate cancer at final pathology. *J. Urol.* **2010**, *184*, 930–937. [[CrossRef](#)] [[PubMed](#)]
50. Zagoria, R.J. *Genitourinary Radiology: The Requisites*; Mosby: Philadelphia, PA, USA, 2004.
51. Elblbesy, M.A. Effect of static magnetic field on erythrocytes characterizations. *J. Biomed. Sci. Eng.* **2010**, *3*, 300–303. [[CrossRef](#)]
52. Chen, P.; Huang, Y.Y.; Hoshino, K.; Zhang, J.X. Microscale magnetic field modulation for enhanced capture and distribution of rare circulating tumor cells. *Sci. Rep.* **2015**, *5*, 8745. [[CrossRef](#)] [[PubMed](#)]
53. Albrecht, M.; Furubayashi, T.; Przybylski, M.; Korecki, J.; Gradman, U. Magnetic step anisotropies. *J. Magn. Magn. Mater.* **1992**, *113*, 207–220. [[CrossRef](#)]
54. Emerson, D.R.; Cieslicki, K.; Gu, X.; Barber, R.W. Biomimetic design of microfluidic manifolds based on a generalised Murray's law. *Lab Chip* **2006**, *6*, 447–454. [[CrossRef](#)] [[PubMed](#)]
55. Lee, A.M.; Tormoen, G.W.; Kanso, E.; McCarty, O.J.; Newton, P.K. Modeling and simulation of procoagulant circulating tumor cells in flow. *Front. Oncol.* **2012**, *2*, 108. [[CrossRef](#)] [[PubMed](#)]
56. Low, W.S.; Kadri, N.A.; Wan Abas, W.A.B.B. Computational fluid dynamics modelling of microfluidic channel for dielectrophoretic biomems application. *Sci. World J.* **2014**, 2014, 11. [[CrossRef](#)] [[PubMed](#)]
57. Berthier, E.; Young, E.W.K.; Beebe, D. Engineers are from pdms-land, biologists are from polystyrenia. *Lab Chip* **2012**, *12*, 1224–1237. [[CrossRef](#)] [[PubMed](#)]
58. Mortensen, N.A.; Okkels, F.; Bruus, H. Reexamination of hagen-poiseuille flow: Shape dependence of the hydraulic resistance in microchannels. *Phys. Rev. E* **2005**, *71*. [[CrossRef](#)] [[PubMed](#)]
59. Feng, J.; Chuncheng, Z.; Peng, Z.; Deyi, Z. Optimization of turn geometries in microfluidic channels. In Proceedings of the 2005 International Conference on MEMS, NANO and Smart Systems, Banff, AB, Canada, 24–27 July 2005; pp. 32–35.
60. Green, J.V.; Kniazeva, T.; Abedi, M.; Sokhey, D.S.; Taslim, M.E.; Murthy, S.K. Effect of channel geometry on cell adhesion in microfluidic devices. *Lab Chip* **2009**, *9*, 677–685. [[CrossRef](#)] [[PubMed](#)]
61. Peeters, F.M.; Jo, D.B. Hybrid magnetic-semiconductor nanostructures. In *Nanostructured Materials and Nanotechnology*; Nalwa, H.S., Ed.; Academic Press: San Diego, CA, USA, 2002; pp. 247–328.
62. Issa, D.; Albeldawi, M.; Lopez, R.; Alkhouri, N. Hematocrit levels and red blood cell indices in patients with nonalcoholic fatty liver disease. *Eur. J. Gastroenterol. Hepatol.* **2014**, *26*, 363–364. [[CrossRef](#)] [[PubMed](#)]
63. Guldiken, R.; Jo, M.C.; Gallant, N.D.; Demirci, U.; Zhe, J. Sheathless size-based acoustic particle separation. *Sensors* **2012**, *12*, 905–922. [[CrossRef](#)] [[PubMed](#)]

